

1 **Atmospherically-forced sea-level variability in western Hudson Bay, Canada**

2
3 Igor A. Dmitrenko^{1,*}, Denis L. Volkov^{2,3}, Tricia A. Stadnyk⁴, Andrew Tefs⁴, David G. Babb¹,
4 Sergey A. Kirillov¹, Alex Crawford¹, Kevin Sydor⁵, and David G. Barber¹

5
6
7 ¹Centre for Earth Observation Science, University of Manitoba, Winnipeg, Manitoba, Canada

8 ²Cooperative Institute for Marine and Atmospheric Studies, University of Miami, Miami,
9 Florida, USA

10 ³NOAA, Atlantic Oceanographic and Meteorological Laboratory, Miami, Florida, USA

11 ⁴Department of Geography, University of Calgary, Calgary, Alberta, Canada

12 ⁵Manitoba Hydro, Winnipeg, Manitoba, Canada

13
14
15
16
17
18
19
20
21
22
23
24
25
26
27
28 *Corresponding author, igor.dmitrenko@umanitoba.ca, 125 Dysart Rd., University of Manitoba,
29 Winnipeg, Manitoba R3T 2N2 Canada

30 **Abstract:** In recent years, significant trends toward earlier breakup and later freeze-up of sea-ice
31 in Hudson Bay have led to a considerable increase in shipping activity through the Port of
32 Churchill, which is located in western Hudson Bay and is the only deep-water ocean port in the
33 province of Manitoba. Therefore, understanding sea-level variability at the Port is an urgent issue
34 crucial for safe navigation and coastal infrastructure. Using tidal gauge data from the Port along
35 with an atmospheric reanalysis and Churchill River discharge, we assess environmental factors
36 impacting synoptic to seasonal variability of sea level at Churchill. An atmospheric vorticity
37 index used to describe the wind forcing was found to correlate with sea level at Churchill.
38 Statistical analyses show that, in contrast to earlier studies, local discharge from the Churchill
39 River can only explain up to 5% of the sea level variability. The cyclonic wind forcing
40 contributes from 22% during the ice-covered winter-spring season to 30% during the ice-free
41 summer-fall season due to cyclone-induced storm surge generated along the coast. Multiple
42 regression analysis revealed that wind forcing and local river discharge combined can explain up
43 to 32% of the sea level variability at Churchill. Our analysis further revealed that the seasonal
44 cycle of sea level at Churchill appears to be impacted by the seasonal cycle in atmospheric
45 circulation rather than by the seasonal cycle in local discharge from the Churchill River,
46 particularly post-construction of the Churchill River diversion in 1977. Sea level at Churchill
47 shows positive anomalies for September-November compared to June-August. This seasonal
48 difference was also revealed for the entire Hudson Bay coast using satellite-derived sea level
49 altimetry. This anomaly was associated with enhanced cyclonic atmospheric circulation during
50 fall, reaching a maximum in November, which forced storm surges along the coast. Complete
51 sea-ice cover during winter impedes momentum transfer from wind stress to the water column,
52 reducing the impact of wind forcing on sea level variability. Expanding our observations to the
53 bay-wide scale, we confirmed the process of wind-driven sea-level variability with (i) tidal-
54 gauge data from eastern Hudson Bay and (ii) satellite altimetry measurements. Ultimately, we
55 find that cyclonic winds generate sea level rise along the western and eastern coasts of Hudson
56 Bay at the synoptic and seasonal time scales, suggesting an amplification of the bay-wide
57 cyclonic geostrophic circulation in fall (October-November), when cyclonic vorticity is
58 enhanced, and Hudson Bay is ice-free.

59 **Keywords:** Hudson Bay; sea level; Churchill River discharge; atmospheric vorticity.

60

61 **1. Introduction**

62 Hudson Bay in northeast Canada is a shallow (mean depth ~ 150 m), semi-enclosed sub-arctic
63 inland sea that is connected to the Labrador Sea through Hudson Strait (Figure 1). The Bay
64 occupies approximately 831,000 km², making it the world's largest inland sea, and is
65 characterized by a high annual volume of river discharge (712 km³; *Déry et al.*, 2005; 2011) and
66 a dynamic seasonal ice cover that exists from November/December to June/July (*Hochheim and*
67 *Barber*, 2010; 2014). The mean circulation in Hudson Bay is comprised of the wind-driven and
68 estuarine components, where the estuarine portion is driven by the riverine water input
69 (*Prinsenber*, 1986a), and the wind-driven portion is attributed to prevailing along-shore winds
70 (e.g., *Ingram and Prinsenber*, 1998; *Saucier et al.*, 2004; *St-Laurent et al.*, 2011; *Ridenour et*

71 *al.*, 2019a; *Dmitrenko et al.*, 2020). Model simulations by *Saucier et al.* (2004) show that the
72 cyclonic circulation is stronger during fall, reaching a maximum in November when the winds
73 are strongest, and weakest in spring when Hudson Bay has a complete sea-ice cover. *Dmitrenko*
74 *et al.* (2020), however, found that even during the ice covered season strong cyclones can
75 amplify water circulation in the Bay. This is consistent with conclusions by *St-Laurent et al.*
76 (2011), who noted that momentum is transmitted through the mobile ice pack to the water
77 column. The efficiency of momentum transmission through the mobile ice strongly depends on
78 sea-ice roughness, which is impacted by ice concentration and characteristic length scales of
79 roughness elements including pressure ridges, melt ponds etc. (e.g., *Lüpkes et al.*, 2012;
80 *Tsamados et al.*, 2014; *Joyce et al.*, 2019). In particular, ice floes in a state of free drift within a
81 partial or weak ice cover, typical of the polynya area in western Hudson Bay, increase the
82 transfer of wind stress into the water column (*Schulze and Pickart*, 2012). Both velocity
83 measurements (*Prinsenber*, 1986b; *Ingram and Prinsenber*, 1998; *Dmitrenko et al.*, 2020) and
84 model simulations (*Wang et al.*, 1994; *Saucier et al.*, 2004; *St-Laurent et al.*, 2011; *Ridenour et*
85 *al.*, 2019b) show that during summer, cyclonic water circulation produces a coastal transport
86 corridor that advects riverine water along the coast toward Hudson Strait and into the Labrador
87 Sea.

88 The local water mass of Hudson Bay is dominated by freshwater input comprised of river runoff
89 from the largest watershed in Canada and sea-ice meltwater (e.g., *Prinsenber*, 1984, 1988,
90 1991; *Saucier and Dionne*, 1998; *Granskog et al.*, 2009; *Eastwood et al.*, 2020). The annual
91 mean discharge rate of $22.6 \times 10^3 \text{ m}^3 \text{ s}^{-1}$ corresponds to a net discharge of 712 km^3 of freshwater
92 per year (*Déry et al.*, 2005, 2011). A similar volume of $742 \pm 10 \text{ km}^3$ of freshwater is contained
93 within the ice pack by April (*Landy et al.*, 2017). Freshwater transport in Hudson Bay exhibits a
94 strong seasonal cycle influenced by the timing of river discharge (e.g., *Déry et al.*, 2005), the
95 annual melt/freeze cycle of sea ice (*Ingram and Prinsenber*, 1998; *Saucier et al.*, 2004; *Straneo*
96 *and Saucier*, 2008; *Granskog et al.*, 2011), and seasonality of wind forcing (*Saucier et al.*, 2004;
97 *St-Laurent et al.*, 2011).

98 During the last decade, significant progress has been achieved in understanding the Hudson Bay
99 environmental system (e.g., *Granskog et al.*, 2009; *Kuzyk et al.*, 2011; *St-Laurent et al.*, 2011;
100 *Piecuch and Ponte*, 2015; *Landy et al.*, 2017; *Kuzyk and Candlish*, 2019; *Eastwood et al.*, 2020;
101 *Dmitrenko et al.*, 2020, 2021). However, the synoptic, seasonal, and interannual variability of sea
102 level in Hudson Bay still remains insufficiently studied due to a scarcity of sea level observations
103 at permanent tidal gauges. Note that the tidal gauge in Churchill (Figure 1) is the only
104 continuously operating tide gauge in Hudson Bay and the central Canadian Arctic. Historically,
105 the focus of sea level studies in Hudson Bay was motivated by this area's post-glacial isostatic
106 rebound (e.g., *Guttenberg*, 1941; *Tushingham*, 1992); for a detailed review of these earlier
107 studies see *Wolf et al.* (2006). The advent of space-geodesy, in particular GPS, absolute-
108 gravimetry, and satellite altimetry measurements (e.g., *Larson and van Dam*, 2000; *Wolf et al.*,
109 2006; *Sella et al.*, 2007) afforded a shift in focus for Hudson Bay sea level research to
110 environmental aspects related to global warming and hydroelectric regulation (*Gough*, 1998,
111 2000), and those associated with increasing the shipping traffic from the Port of Churchill

112 through Hudson Bay to Hudson Strait, which may soon become a federally-designated
113 transportation corridor (e.g., *Andrews et al.*, 2017; *Pew Charitable Trusts*, 2016).

114 In 2016, the University of Manitoba and Manitoba Hydro launched a project on “Variability and
115 change of freshwater-marine coupling in the Hudson Bay System”, named BaySys, which aimed
116 to assess the relative contributions of climate change and river regulation to the Hudson Bay
117 system. Here, we are specifically focused on the impact of the Churchill River diversion on
118 variability of sea level at the Port of Churchill. Additionally, we put our findings in the context of
119 wind forcing over the entire Hudson Bay, elaborating on the suggestion by *Dmitrenko et al.*
120 (2020) that cyclonic wind forcing generates onshore Ekman transport and storm surges along the
121 coast.

122 We also revisit earlier results by *Gough and Robinson* (2000) and *Gough et al.* (2005). Using
123 tidal gauge and river discharge data from 1974 to 1994, *Gough and Robinson* (2000) suggested
124 that the Churchill River discharge dominates sea-level variability at Churchill. They explained
125 the seasonal elevation of sea level during late fall by a recirculating mechanism that links the
126 spring pulse of river discharge in the downstream James Bay (Figure 1) to sea level at Churchill
127 (*Gough and Robinson*, 2000; *Gough et al.*, 2005). In this paper, we present an alternative
128 mechanism and show that (i) the Churchill River discharge plays a secondary role for generating
129 sea level anomalies at Churchill, and (ii) the synoptic and seasonal variability of sea level at
130 Churchill and over the entire Hudson Bay is impacted by the wind forcing described with an
131 atmospheric vorticity index (Figure 2).

132

133 **2. Data**

134 *2.1. Sea level*

135 The daily mean sea level data used in this study were retrieved from the Canadian Tides and
136 Water Levels Data Archive of the Fisheries and Oceans Canada through [http://www.isdm-
137 gdsi.gc.ca/isdm-gdsi/twl-mne/index-eng.htm#s5](http://www.isdm-gdsi.gc.ca/isdm-gdsi/twl-mne/index-eng.htm#s5) (last access: 26 August 2021). Sea level data
138 were de-tided using an algorithm by *Foreman* (1977). Measurements of sea level at Churchill
139 were obtained from the permanent tidal gauge that is installed at the port of Churchill (station
140 #5010) near the mouth of the Churchill River (Figure 1). While measurements of sea level at
141 Churchill date back to the 1930s (*Gutenberg*, 1941), we only used data from 1950 to present
142 (Figure 3a), which is coincident with atmospheric reanalysis data from the National Centers for
143 Environmental Prediction (NCEP; *Kalnay et al.*, 1996). In addition, we used sea level data from
144 the temporary tidal gauge in Inukjuak (station #4575), Cape Jones Island (station #4656), and
145 North Kopak Island (station #4548) (Figure 1). Among these three locations, only data at
146 Inukjuak are fully representative for our analysis because they span a sufficiently long period
147 from October 1969 to October 1980, however, only the portion of this time series from
148 September 1973 to December 1975 is continuous. Sea level records at Cape Jones Island and
149 North Kopak Island are from August-October 1973 and 1975, respectively, and were selected
150 among other temporary stations in Hudson Bay to overlap with sea level time series at
151 Inukjuak.

152 Satellite altimetry data from 1993-2020 were used to analyze the relationship between wind
153 forcing and sea level changes over the entire Hudson Bay. We used the daily fields of absolute
154 dynamic topography (ADT), i.e. the sea surface height above geoid, processed and distributed by
155 Copernicus Marine and Environment Monitoring Service (CMEMS;
156 <https://marine.copernicus.eu/>; last access: 26 August 2021). The ADT is obtained by adding a
157 mean dynamic topography (DT2018, *Mulet et al.*, 2013) to sea level anomaly (SLA) measured
158 by altimetry satellites. The CMEMS SLA/ADT fields are computed by optimally interpolating
159 data from all satellites available at a given time following a methodology described in *Pujol et*
160 *al.* (2016). Prior to mapping, altimetry records are corrected for instrumental noise, orbit
161 determination error, atmospheric refraction, sea state bias, static and dynamic atmospheric
162 pressure effects, and tides. Because in this work we are interested in local (dynamic) changes of
163 sea level, the global mean sea level was subtracted from each ADT map. Then the seasonal
164 climatology was computed for June through August (JJA) and September through November
165 (SON) by averaging all available maps during the respective seasons. Sea ice does not represent
166 a significant problem for computing the climatology, because Hudson Bay is essentially ice free
167 during these months, especially during SON.

168 The root-mean-square differences between tide gauge records and collocated SLA/ADT data are
169 usually 3-5 cm (e.g., *Volkov et al.*, 2007; *Pascual et al.*, 2009; *Volkov et al.*, 2012) and do not
170 exceed 10 cm globally (*CLS-DOS*, 2016). When the altimetry data are averaged to produce the
171 seasonal climatology, the measurement error is greatly reduced (at least by an order of
172 magnitude for 28 years of altimetry record). It should be noted that altimetry errors near the coast
173 are greater than in the open ocean. This is due to land contamination within the radar footprint
174 and to the fact that the geophysical corrections applied to altimetry data are usually optimized for
175 the open ocean and not for the coastal zones. In classical altimetry products, however, a large
176 percentage of data within 10–15 km from the coast is deemed invalid and not used for generating
177 SLA/ADT maps (e.g., *The Climate Change Initiative Coastal Sea Level Team*, 2020).
178 Furthermore, satellite altimetry data was used here only for a qualitative assessment of the basin-
179 scale seasonal sea-level patterns in Hudson Bay. Therefore, the reduced quality of altimetry
180 retrievals near the coast is not expected to impact the conclusions of this study.

181 2.2. River discharge

182 Churchill River discharge data were obtained from *Déry et al.* (2016) and extended to 2019;
183 thus, we use a continuous record of daily mean discharge from 1960 to 2019 (Figure 4a and
184 supplementary material). The record was constructed from gauged observations above Red Head
185 Rapids (station #06FD001), which is located ~87 km from the Churchill River mouth and is the
186 most downstream hydrometric gauge along the Churchill River. When these data were not
187 available, we used upstream gauges (applying a drainage area correction) to fill significant gaps
188 in the time series (see *Déry et al.* 2005 for detailed methods). Data were adjusted by drainage
189 area (between the hydrometric gauge location and river outlet) and any significant tributary
190 inflows were added to represent discharge at the outlet of the Churchill River.

191 2.3. Wind forcing

192 Fields of sea level pressure (SLP) and 10-m wind velocity at 6-h intervals were derived from the
193 NCEP atmospheric reanalysis (<https://psl.noaa.gov/data/composites/hour/>; last access: 26 August
194 2021). We chose the NCEP reanalysis to extend the atmospheric forcing data back to 1950,
195 which covers the tide gauge record from Churchill, while a previous comparison of wind speeds
196 from NCEP and ERA5 (*Copernicus Climate Change Service, 2017; Hersbach et al., 2020*) with
197 in situ observations from the Churchill weather station revealed an insignificant discrepancy
198 between the two reanalyses and meteorological observations (*Dmitrenko et al., 2020*). However,
199 we used the ERA5 SLP data to validate atmospheric vorticity derived from NCEP as described
200 below in section 3. For simplicity, cyclones over the Hudson Bay area were manually tracked for
201 August-May 1969-1970 and 2003-2004 using the NCEP SLP fields, with the central position and
202 low SLP tabulated. The horizontal resolution of the NCEP-derived data is 2.5° of latitude and
203 longitude.

204 For the majority of tidal gauge data from 1950s, sea level at Churchill was recorded hourly. In
205 contrast, the Churchill River discharge from gauged observations above Red Head Rapids
206 (station #06FD001) is available daily. The NCEP data on SLP and 10-m wind are available at 6-
207 h intervals. To make these three time series comparable, we analyzed daily means.

208

209 **3. Methods**

210 For the 1950/60–2019 study period, a vorticity index was derived from the daily mean SLP
211 NCEP data to characterize the wind forcing and compare to the time series of sea level anomalies
212 (Figures 2a, 3a, and 4a). The vorticity index gives both the sign and magnitude of atmospheric
213 vorticity; it was first proposed by *Walsh et al. (1996)* and then successfully used for describing
214 atmospheric forcing over the Siberian shelves (*Dmitrenko et al., 2008a; 2008b*) and Hudson Bay
215 (*Dmitrenko et al., 2020*). The vorticity index is defined as the numerator of the finite difference
216 Laplacian of SLP for an area within a radius of 550 km centered at 60°N and 85°W in Hudson
217 Bay (Figure 1). A positive index corresponds to cyclonic atmospheric circulation that is typically
218 associated with northerly winds in western Hudson Bay, whereas a negative vorticity index
219 corresponds to anticyclonic atmospheric circulation characterized by southerly winds in western
220 Hudson Bay (Figure 2). *Dmitrenko et al. (2020)* examined the spatial uncertainty of atmospheric
221 vorticity estimated at 60°N , 85°W by computing vorticity for the 5-point stencils with a central
222 node shifted relative to 60°N , 85°W by approximately 280 km northward, eastward, southward,
223 and westward. Their results show that vorticity computed at 60°N , 85°W best describes major
224 cyclonic storms observed in 2016–2017.

225 The vorticity index used in this study does not fully explain the observed variability of
226 meridional wind in western Hudson Bay (Figure 2b), which is mainly responsible for generating
227 storm surge along the coast (*Dmitrenko et al., 2020*). However, vorticity describes the intensity
228 of cyclonic wind forcing over the entire Bay impacting the basin-scale circulation and sea level
229 deformations along the entire coastline of Hudson Bay (*Dmitrenko et al., 2020*). Thus, our
230 approach allowed us to extend our findings over the entire Bay. We also conducted a validation
231 comparing the NCEP-derived vorticity to that derived from the ERA5 SLP utilizing the Web-

232 Based Reanalysis Intercomparison Tools (<https://psl.noaa.gov/cgi-bin/data/testdap/timeseries.pl>;
233 last access: 26 August 2021) described by *Smith et al.* (2014). The comparison showed
234 insignificant differences between the two reanalyses: the NCEP-derived vorticity only slightly
235 exceeds that obtained from ERA5, while the correlation between the NCEP and ERA5-derived
236 vorticities is 0.96 (Figure 2a).

237 The Churchill River discharge time series (Figure 4a) was compiled as follows. First, no
238 significant gaps in Churchill River discharge record occurred on a daily basis. There were,
239 however, some missing discharge data between 1976 and 1995, with some gaps up to 3 months
240 (e.g., 1984, 1987). When data gaps occurred, then the upstream hydrometric gauge below Fidler
241 Lake (station #06FB001) was used to infill data, with streamflow data adjusted to account for the
242 difference in contributing area between Fidler Lake and the Churchill outlet, following the
243 procedure of *Déry et al.* (2005). When the upstream hydrometric data were also unavailable, a
244 secondary step was taken to infill data gaps. Missing data on a given day were infilled using the
245 day-of-year mean value of streamflow over the available period of record. This procedure
246 constructed a daily climatology of streamflow (i.e., mean annual hydrograph) based on the
247 availability of data over the period of record.

248 For the Churchill River, however, we constructed a separate climatology of daily streamflow for
249 the periods prior to and after flow diversion in 1977. Partial diversion began in 1976, allowing
250 less than the full capacity of discharge to be diverted into the Nelson River system, with full
251 operation beginning in 1977. We therefore designated 1977 as the first year when diversion
252 became operational.

253 It is also important to separate the pre- and post-regulation periods for the analysis of the
254 potential impact natural (pre-diversion) and regulated Churchill River discharge have on sea
255 level anomalies at Churchill. *Déry et al.* (2016) reported that the Churchill River diversion
256 caused a significant decline in the mean annual discharge from $37.0 \pm 4.2 \text{ km}^3 \text{ year}^{-1}$ pre-
257 diversion (1964–73) compared to post-diversion flows (8.4 ± 2.9 and $9.6 \pm 4.4 \text{ km}^3 \text{ year}^{-1}$ for
258 1984–93 and 1994–2003, respectively). *Déry et al.* (2016) further revealed the coefficient of
259 variation (CV) of annual Churchill River discharge increased in inter-decadal CV post-diversion
260 (1984–2013; $\text{CV} = 0.35\text{--}0.67$) compared to pre-diversion records (1964–1973; $\text{CV} = 0.11$). Both
261 the decline in mean annual discharge and increase in discharge variability for the post-diversion
262 period necessitate separate analysis of the impact of river discharge on sea level variability due
263 to non-stationarity in the discharge record, which was implemented in our analysis.

264 The sea level record in Churchill is impacted by the post-glacial isostatic adjustment, with
265 present-day uplift in the Hudson Bay area of $\sim 10 \text{ mm year}^{-1}$ (e.g., *Sella et al.*, 2007). Combining
266 satellite altimeter data with the Churchill tide-gauge data gives an uplift rate of about 9.0 ± 0.8
267 mm year^{-1} (*Ray*, 2015). The crustal uplift is evident in the negative sea level trend at Churchill of
268 about the same magnitude (Figure 3a). To examine synoptic to seasonal variability of sea level at
269 Churchill, a polynomial fit was subtracted from the data (Figure 3a). The polynomial fit better
270 explains long-term variability of sea level at Churchill compared to the linear approximation,
271 with respective coefficients of determination (R^2) of 0.41 and 39. Thus, in our study we
272 examined the sea level anomalies (SLA) against the low-frequency trend conditioned by the

273 post-glacial isostatic adjustment. In addition, the inverse barometer contribution to the water
274 level record was removed using sea-level atmospheric pressure from the NCEP reanalysis. The
275 mean correction attributed to inverted barometer effect was -1.19 ± 8.72 cm.

276 We used multiple linear regression to estimate a partial contribution of the cyclonic wind forcing
277 and Churchill River discharge to SLA. In this context, multiple regression uses the least squares
278 method to calculate the value of SLA based on the two independent variables as the vorticity
279 index and Churchill River discharge.

280

281 **4. Results**

282 In this section, we examine the impact of wind forcing and local river discharge on sea level
283 variability at Churchill. We analyze (4.1) SLA at Churchill, (4.2) atmospheric vorticity over
284 Hudson Bay, (4.3) the Churchill River discharge, and (4.4) their correlations.

285 *4.1. Sea level*

286 The 30-day running mean of SLA at Churchill ranging from 0.39 m in October 1973 to -0.36 m
287 in April 1981 is dominated by the seasonal cycle (Figure 4a, blue line). In terms of the long-term
288 monthly mean, sea level shows a seasonal cycle with positive anomalies > 0.09 m from
289 September-November and negative anomalies of about -0.14 m from March-April (Figure 5a).

290 There is a substantial difference in the seasonal patterns of sea level between the pre- and post-
291 diversion periods. The long-term variability of sea level (Figure 3a) and SLA (Figure 4a) shows
292 no abrupt disruption with the introduction of the Churchill River diversion in 1977. However, the
293 seasonal cycle of SLA generated for pre- and post-diversion shows a characteristic difference in
294 the timing and magnitude of SLA (Figure 5a). First, for the natural seasonal cycle prior to 1977
295 (blue line in Figure 5a), SLA shows two seasonal peaks in June (~ 0.04 m; standard error of the
296 mean $\sigma = \pm 0.01$ cm) and November (~ 0.11 m, $\sigma = \pm 0.02$ cm). Post-diversion, SLA shows no
297 peak in June, but the magnitude of positive anomalies in September and October increased to $>$
298 0.08 m. This result is consistent with findings by *Gough and Robinson* (2000). In contrast to
299 summer, during February-May, the pre- and post-diversion magnitude of SLA decreased and
300 increased, respectively, by $\geq \pm 0.02$ m relative to the long-term monthly mean (Figure 5a). The
301 standard deviation of the monthly mean values is up to 0.1 m (error bars in Figure 5a). The
302 seasonal pattern of SLA was partially disrupted in 1981-82 and 1987-88, and significantly
303 diminished in 1962-63 and 2016-17 (Figures 3a and 4a).

304 A closer look at the daily data reveals that the sea level seasonal maximum from October-
305 November is modulated by storm surges frequently observed during the late fall. For example, in
306 1969-70 and 2003-04 (highlighted with yellow shading on Figure 4), the seasonal cycle of sea
307 level (Figure 6, thick light blue line) was impacted by synoptic-scale events dominant during
308 October-November (Figure 6, blue line). These storm surges lasted from ~ 3 to 6 days and
309 correspond to positive anomalies of up to 0.5 m in the daily mean sea level (Figure 6b). In
310 contrast, from December to May, the number and magnitude of storm surges gradually decrease
311 (Figure 6).

312 4.2. *Wind forcing*

313 The vorticity index shows predominant cyclonic atmospheric circulation over Hudson Bay
314 (mostly positive values in Figure 3a, red line), which agrees with results presented by *Saucier et*
315 *al.* (2004) and *St-Laurent et al.* (2011). The strongest positive (cyclonic) vorticity is observed
316 from fall 1962 to winter 1963 (vorticity index exceeded 14 s^{-1}), while the strongest negative
317 (anticyclonic) atmospheric forcing (vorticity $< 4 \text{ s}^{-1}$) is recorded during summer 1963 (Figure
318 3a). Overall, the alternation between monthly mean cyclonic and anticyclonic wind forcing is
319 mostly governed by the seasonal cycle in vorticity (Figure 5b). The monthly mean vorticity
320 increases from 4 s^{-1} in September to $\sim 8 \text{ s}^{-1}$ in November, and then gradually returns to $\sim 4 \text{ s}^{-1}$ in
321 February (Figure 5b). During March-May and August, vorticity is relatively low ($< 2 \text{ s}^{-1}$), and
322 only in June and July does vorticity change to weak anticyclonic (slightly negative) values
323 (Figure 5b). The seasonal cycle in atmospheric vorticity shows an insignificant difference pre-
324 and post-diversion. From May to August and in December, there is no difference between the
325 long-term monthly mean and monthly mean estimates for pre- and post-diversion (Figure 5b).
326 For other months, the difference does not exceed $\pm 0.7 \text{ s}^{-1}$.

327 The interannual variability of wind forcing is mainly attributed to year-to-year changes in the
328 cyclonic atmospheric circulation during fall-winter months. The seasonal amplitude of vorticity
329 is significantly diminished in 1953-54, 2001-02 and 2015-2016 when the seasonal mean vorticity
330 index for late fall to the beginning of winter did not exceed 8 s^{-1} (black triangles in Figure 3a). In
331 contrast, during 1960-65, the vorticity seasonal cycle is amplified with the seasonal mean
332 vorticity index between late fall and early winter up to 28 s^{-1} (green triangles in Figure 3a). The
333 standard deviation of the monthly mean vorticity shown by error bars in Figure 5b gradually
334 decreases from $\pm 4.5 \text{ s}^{-1}$ in December to $\pm 2.8 \text{ s}^{-1}$ in March-April.

335 Analysis of the daily vorticity time series sheds light on the origin of seasonality in vorticity.
336 Positive seasonal anomalies from September-December (Figures 3a and 5b) are partly attributed
337 to the occurrence of numerous vorticity peaks. For example, in 1969-70 and 2003-04
338 (highlighted with yellow shading in Figure 3), the seasonal enhancement of atmospheric vorticity
339 (Figure 6, thick pink line) was partially conditioned by synoptic-scale events recorded during
340 October-November 1969 and 2003 (Figure 6, red line). The strongest vorticity peaks were
341 observed on 18 October and 25 November 1969 ($> 4 \text{ s}^{-1}$; Figure 6a) and 15 October and 21
342 November 2003 ($> 5 \text{ s}^{-1}$; Figure 6b). The SLP spatial distribution reveals that each of these peaks
343 is attributable to a cyclone passing over Hudson Bay, with the center of low SLP located over the
344 central Hudson Bay on 18 October and 25 November 1969 (Figures 7a and 7b, respectively) and
345 15 October and 21 November 2003 (Figures 7c and 7d, respectively). The horizontal gradients of
346 SLP over western Hudson Bay ranged from $0.020 \text{ hPa km}^{-1}$ (25 November 1969; Figure 7b) to
347 $0.035 \text{ hPa km}^{-1}$ (21 November 2003; Figure 7d). Overall, from 1 September to 31 December,
348 vorticity exceeded 2 s^{-1} nine and 12 times in 1969 and 2003, respectively. In contrast, from 1
349 January to 30 April 1970 and 2004, vorticity exceeded 2 s^{-1} only four and seven times,
350 respectively (Figure 6). This suggests that the seasonal cycle in atmospheric vorticity is partially
351 governed by the number and strength of cyclones passing over Hudson Bay.

352 4.3. *Local river discharge*

353 The time series of Churchill River discharge (Figure 4a) is dominated by (i) the introduction of
354 the flow diversion in 1977 and (ii) the seasonal hydrologic cycle. The mean discharge dropped
355 by about one-third from $1,190 \text{ m}^3 \text{ s}^{-1}$ (1960-1976) to about $400 \text{ m}^3 \text{ s}^{-1}$ following the diversion in
356 1977. At the same time, the standard deviation of the mean discharge increased from about ± 300
357 to $\pm 470 \text{ m}^3 \text{ s}^{-1}$ following the diversion (Figure 4a). This is in line with results by *Déry et al.*
358 (2016). The mean annual timing of maximum river discharge during late spring to summer is not
359 significantly disrupted by the diversion (Figure 5c). The magnitude of the monthly mean
360 discharge pre- to post-diversion, however, reduces from about five-fold in March to about two-
361 and-a-half-fold in May-August (Figure 5c). After diversion, the standard deviation of the
362 monthly mean discharge doubles from May to October (Figure 5c). In contrast, from December
363 to April, the standard deviation of the monthly mean was not significantly impacted by the
364 diversion (Figure 5c).

365 4.4. Sea level response to wind forcing and local river discharge

366 Our data shows that SLA in Churchill, atmospheric vorticity over Hudson Bay, and Churchill
367 River discharge all show variability dominated by the seasonal cycle (Figures 3a, 4a, and 5). In
368 what follows, SLA at Churchill is first compared to the atmospheric vorticity, and then to the
369 Churchill River discharge, with a main focus on the seasonal cycle.

370 The correlation between the daily vorticity index and SLA from 1950-2019 and 1960-2019 is
371 0.48 and 0.47, respectively, with insignificant differences between correlations estimated for
372 periods pre- and post-diversion (0.49 and 0.47, respectively; Figure 3b and Table 1). For the ice-
373 free period from June to November, correlations for whole period, and pre- and post-diversion
374 increase to 0.54, 0.52 and 0.55 (Table 2), respectively, compared to 0.47, 0.49 and 0.47 for the
375 ice-covered period from December to May (Table 3). We test the difference between correlations
376 estimated for the ice-covered and ice-free seasons using the Fisher z-transformation (*Fisher,*
377 1921). Statistical assessment shows that the only differences between correlations estimated for
378 whole period and post-diversion are statistically significant at the 99% confidence level.

379 The relationship between vorticity and SLA changes significantly from one year to another. The
380 mean annual correlations in Figure 3b show these differences ranging from 0.18 in 1982 to 0.69
381 in 1991. During periods when the sea level seasonal cycle almost disappears (1981-82 and 1987-
382 88), the mean annual correlation drops to about 0.3 and 0.4, respectively (Figure 3b). When the
383 sea level seasonal cycle is diminished (1962-63 and 2016-17), a modest correlation of ~ 0.5 is
384 estimated (Figure 3b). For time periods enlarged in Figure 6, the annual mean correlation
385 significantly exceeds the long-term mean of 0.47, attaining 0.65 and 0.57 for 1969-70 and 2004-
386 05, respectively (Figure 3b). The direct linkage between vorticity and SLA is evident in Figure 6.
387 During September-November 1969 and 2003, all significant synoptic peaks in SLA are
388 consistent with those in atmospheric vorticity, including storm surges on 18 October and 25
389 November 1969 (Figure 6a) and on 15 October and 21 November 2003 (Figure 6b).

390 In contrast to atmospheric vorticity, the correlation between daily SLA and river discharge is
391 significantly smaller. Through the full record from 1960 to 2019, the correlation is 0.22, with an
392 insignificant difference between pre- and post-diversion (0.20 and 0.23, respectively, Figure 4b)

393 and Table 1). For the ice-free period from June to November, correlations drop close to or below
394 the level of statistically significant values for the whole and pre-diversion periods (0.08 and 0.03,
395 respectively), and to 0.11 post-diversion (Table 2) compared to 0.21, 0.12 and 0.19 for the ice-
396 covered period from December to May (Table 3). Note that the difference between correlations
397 estimated for the ice-covered and ice-free seasons is statistically significant for only 1960-2019.

398 Similar to the linkage between vorticity and SLA, the relationship between river discharge and
399 SLA shows significant interannual variability. Correlations computed through the 365-day
400 moving window show negative to positive values ranging from -0.3 to 0.7 with about 15% of
401 estimates below the level of statistical significance (Figure 4b). Among all events when the
402 amplitude of the sea level seasonal cycle was strongly reduced, only 1962-63 and 1981-82 show
403 statistically significant correlation between river discharge and SLA of ~ 0.25 (Figure 4b). For
404 events in 1987-88 and 2016-17, correlation is relatively close to or below the level of statistical
405 significance (Figure 4b). The interannual difference in contribution of river discharge to the sea
406 level variability is also evident for 1969-70 and 2004-05. In 1969-70, the annual mean
407 correlation shows relatively modest contributions of river discharge to sea level variability
408 (correlation $R \sim 0.29$; Figure 4b) as compared to correlation with atmospheric vorticity ($R \sim 0.65$;
409 Figure 3b). In 2004-05, however, there is no correlation between SLA and river discharge
410 (Figure 4b), and sea level variability is impacted by wind forcing ($R = 0.57$; Figure 3b).

411 Overall, our results show that the wind forcing impacts the synoptic and seasonal variability of
412 sea level. In what follows, we use the coefficient of determination (R^2 , where R is correlation
413 coefficient in Tables 1-3) to describe the proportion of the variance in sea level that is explained
414 by the wind forcing, river discharge, and the wind forcing and river discharge together. Through
415 the whole annual cycle from 1960 to 2019, wind forcing explains about 22% of sea level
416 variability, while river discharge contributes only $\sim 5\%$. Multiple regression analysis shows that
417 on average, both explain $\sim 28\%$ of sea level variability (Table 1).

418 Our results also reveal the important role of sea-ice cover and river diversion in modifying
419 controls on sea level variability. During the ice-free seasons from 1960-1976, the contribution of
420 wind forcing is 27%, and the role of river discharge is negligible (Table 2). Post-diversion,
421 cyclonic wind forcing and river discharge contribute 30% and 1%, respectively. Together they
422 explain up to 32% of sea level variability (Table 2). During the ice-covered season, the
423 contribution of vorticity is reduced to 22%, with insignificant difference between pre- and post-
424 diversion (Table 3). The contribution of river discharge varies from 1% for pre-diversion to 4%
425 for post-diversion. Wind and river forcing together explain $\sim 27\%$ of sea level variability for both
426 pre- and post-diversion periods (Table 3). Summarizing these results, we point out that the sea-
427 ice cover reduces the influence of wind forcing, and the influence of local river discharge is
428 slightly increased primarily during the ice covered post-diversion period. Post-diversion, the
429 magnitude of river discharge was reduced about three-fold, but seasonal variability increased by
430 a factor of 1.5 (Figure 4a and *Déry et al.*, 2016). Thus, we attribute the increase in river
431 discharge forcing during the post-diversion period mainly to the higher variability in river
432 discharge from May to November (Figure 4a, 5c, and *Déry et al.*, 2016). Note that during May
433 about 85% of Hudson Bay is ice covered (*Tivy et al.*, 2010), and the standard deviation of the

434 monthly mean discharge in May increases from about ± 170 pre-diversion to ± 380 $\text{m}^3 \text{s}^{-1}$ post-
435 diversion.

436

437 5. Discussion

438 Our results show that sea level variability at Churchill is rather influenced by wind forcing, with
439 discharge from the Churchill River playing a secondary role. Overall, the atmospheric vorticity
440 explains up to 30% of sea level variability at Churchill, with local river discharge contributing up
441 to only 5% (Tables 1-3). This suggests that in western Hudson Bay the northerly winds
442 associated with cyclonic wind forcing (Figure 2b) generate storm surge along the coast due to a
443 surface Ekman on-shore transport. This is consistent with results from *Dmitrenko et al.* (2020),
444 who used mooring records and Churchill tide gauge observations in 2016-17 to identify this
445 mechanism. A direct response of the water level to balance wind stress acting on the surface does
446 not play a role for generating SLA because there is no correlation between SLA and zonal wind
447 (not shown).

448 The SLA seasonal cycle in Figure 5a is only partially explained by seasonality in wind forcing
449 and local river discharge. The SLA seasonal cycle is also consistent with summertime warming
450 and freshening, and wintertime cooling and salinification. During the ice-free summer period, the
451 water column warms, and seawater becomes less dense and expands, causing the thermosteric
452 sea-level rise. In addition, during summer, riverine water and sea-ice meltwater decrease salinity
453 of the Bay, thus, causing the halosteric sea-level rise. It seems that these factors can explain the
454 significant fraction of the SLA seasonal variability that is not explained by wind forcing and
455 local river discharge. However, the detailed assessment of the thermosteric and halosteric
456 contributions to the Hudson Bay sea level variability is beyond the scope of this paper. In this
457 context, we point out that we examine only the direct impact of the river discharge on the sea
458 level in the Churchill River mouth ignoring the cumulative effect of riverine water on steric
459 height. This simplification seems to be reasonable because the residence time of the riverine
460 water fraction in southwestern Hudson Bay during summer is ~ 1 -3 months (*Granskog et al.*,
461 2009).

462 For the seasonal time scales, increased cyclonic activity during fall to early winter impacts the
463 seasonal cycle in SLA. In contrast to *Gough and Robinson* (2000), we assert that a positive SLA
464 from September-November (Figure 5a) is attributed to enhanced atmospheric vorticity rather
465 than to the local river discharge. The signature of the local river discharge is, however, traceable
466 through the SLA seasonal cycle. During the pre-diversion period, positive SLA in June (Figure
467 5a) appears to be linked to the spring freshet of the Churchill River (Figures 5a and 5c).
468 However, post-diversion this positive SLA in June vanishes due to the abrupt decrease in the
469 Churchill River discharge during the spring freshet from $\sim 1,500$ to 700 $\text{m}^3 \text{s}^{-1}$ (Figure 5c).
470 Gradual decreases in Churchill River discharge from June/July to April for both pre- and post-
471 diversion cannot explain the positive SLA from fall to winter, especially during the post-
472 diversion period when the mean annual Churchill River discharge decreases to ~ 400 $\text{m}^3 \text{s}^{-1}$
473 (Figure 5c). Note that the cumulative effect of riverine water on steric height is neglected.

474 An additional perspective on SLA response to atmospheric and river forcing comes from a
475 comparison of the monthly mean vorticity and Churchill River discharge time series with SLA at
476 Churchill for the whole period of river discharge observations, and the pre- and post-diversion
477 periods (Figures 8a, 8b, and 8c, respectively). The SLA patterns for the whole period of river
478 discharge observation (Figure 8a) are strongly impacted by changes in the magnitude of
479 discharge during the pre- and post-diversion periods, as previously discussed. In contrast, the
480 SLA patterns compiled for the pre- and post-diversion periods (Figures 8b and 8c, respectively)
481 provide more precise features of the SLA response to atmospheric and river forcing. In general,
482 comparing atmospheric vorticity to sea level at Churchill shows that cyclones generate positive
483 SLA up to 0.15 m (Figure 8c). The maximum SLA response to cyclonic atmospheric forcing is
484 observed during the ice-free period (pink shading and white circles in Figures 8b and 8c), which
485 is consistent with results of the correlation analysis (Tables 2 and 3). The combination of
486 anticyclonic (negative) vorticity and low river discharge generates negative SLA up to 0.09 m
487 during both ice-free and ice-covered seasons (blue shading in Figures 8b and 8c).

488 The zero SLA contour in Figure 8b and 8c is displaced relative to the zero vorticity and the long-
489 term mean river discharge for the pre- and post-diversion periods. This indicates that these two
490 predictors alone are insufficient to entirely explain the sea level variability, and that there must
491 be other contributing factors. Correlation analysis (Tables 2 and 3) suggests that sea-ice also
492 plays a role in modifying the impact of atmospheric forcing on SLA. In this context, Figures 8
493 reveals the role of sea-ice cover for generating the SLA. The sea level at Churchill exhibits
494 negative SLA while atmospheric vorticity is positive, but not exceeding $\sim 6\text{-}8\text{ s}^{-1}$ (Figure 8). This
495 situation is usually observed during the ice-covered season when river discharge is below the
496 annual mean (blue circles and blue shading in Figures 8b and 8c). We attribute this disruption to
497 the sea-ice cover. Throughout the entire year, positive SLA is generated in response to strong
498 cyclones with vorticity exceeding $\sim 6\text{-}8\text{ s}^{-1}$ regardless of the river discharge contribution and sea-
499 ice conditions (red shading in Figure 8 for vorticity $>\sim 6\text{-}8\text{ s}^{-1}$). During the ice-covered season, at
500 relatively low river discharge ($<1,200\text{ m}^3\text{ s}^{-1}$ and $350\text{ m}^3\text{ s}^{-1}$ for pre- and post-diversion,
501 respectively), negative SLA is associated with positive vorticity $<6\text{-}8\text{ s}^{-1}$ (blue circles and blue
502 shading in Figures 8b and 8c). Thus, vorticity $\sim 6\text{-}8\text{ s}^{-1}$ is suggested to be a very rough estimate of
503 the vorticity threshold attributed to the sea-ice impact. Above this threshold, sea-ice does not
504 eliminate wind stress from the water column, and wind forcing impacts sea level variability in
505 Churchill year-round. Below this threshold, sea-ice eliminates wind forcing and a negative SLA
506 is conditioned by low river discharge. In fact, extension of the landfast ice as well as sea-ice
507 roughness and concentration can play a role modifying the thresholds at which wind impacts the
508 SLA. When the Churchill River discharge exceeds the monthly means of $1,500\text{-}1,600\text{ m}^3\text{ s}^{-1}$ and
509 $\sim 900\text{ m}^3\text{ s}^{-1}$ for pre- and post-diversion periods, respectively, positive SLA results regardless of
510 wind forcing.

511 Our results on the mechanisms of sea level variability at Churchill differ from those obtained by
512 *Gough and Robinson* (2000). First, using sea level and river discharge data from 1974-1994, they
513 found that correlation between Churchill River discharge and SLA in Churchill explains 43% of
514 sea level variability (versus the 5% derived in our analysis). Second, *Gough and Robinson*
515 (2000) explain a positive SLA observed in Churchill from October-November by the river

516 discharge pulse into the James Bay region with an advective lag of ~4-5 months. Furthermore,
517 *Gough et al.* (2005) speculate that positive SLA during fall is attributed to the James Bay
518 riverine water fraction, which does not exit the Bay through Hudson Strait, but instead re-
519 circulates in western Hudson Bay. The halosteric sea level changes associated with this
520 freshwater fraction are suggested to generate a positive SLA observed in Churchill from
521 October-November. The pathway of this water and the reason for disrupting the mean cyclonic
522 circulation in the Bay were, however, neither specified in *Gough and Robinson* (2000) nor in
523 *Gough et al.* (2005). The distance from James Bay to Churchill measured along the coast is
524 roughly 1,000 km. For a 120-150-day lag between peaks in river discharge to James Bay in June
525 (*Déry et al.*, 2005) and maximum positive SLA at Churchill in November, this distance suggests
526 the unrealistic rate of mean advective velocity to be ~8-10 cm s⁻¹. Note that *Dmitrenko et al.*
527 (2020) estimated the velocity of the northward flow along the western coast of Hudson Bay
528 during strong cyclonic storms to ~13 cm s⁻¹, which significantly exceeds the annual mean
529 meridional transport of ~1-2 cm s⁻¹.

530 Overall, the hypothesis by *Gough and Robinson* (2000) and *Gough et al.* (2005) about the
531 linkage between the river discharge pulse into James Bay and a positive SLA in Churchill is
532 suggestive of the seasonal disruption of the Hudson Bay cyclonic circulation that is in line with
533 the seasonal pattern of atmospheric vorticity in Figure 5b. Based on satellite altimetry and
534 numerical simulation, *Ridenour et al.* (2019a) revealed a seasonal reversal to anticyclonic
535 circulation in southwestern Hudson Bay from May-July, with a return to strong cyclonic
536 circulation in fall in response to the seasonal patterns of surface stress. This is consistent with the
537 seasonal cycles of vorticity presented in Figure 5b. However, among ~120-150 days of the
538 hypothetical transit time from James Bay to Churchill, the anticyclonic atmospheric forcing is
539 persistently observed only during May-July; in August, vorticity returns to cyclonic (Figure 5b).
540 In the three months before the occurrence of the positive SLA at Churchill in November, the
541 atmospheric forcing has already returned to cyclonic (Figure 5b). In this context, the hypothesis
542 by *Gough and Robinson* (2000) and *Gough et al.* (2005) linking SLA in Churchill to river
543 discharge in James Bay seems to be inconsistent. In what follows, we provide additional
544 arguments to support our finding on the role of wind forcing in generating the SLA at Churchill.

545 First, *Tushingham* (1992) provide the time series of sea level at Churchill and the Churchill River
546 discharge from 1972 to 1989 (Figure 5 from *Tushingham*, 1992). These time series clearly show
547 an overall low positive correlation completely disrupted in 1973-74, 1977, and 1987-86, which is
548 consistent with our analysis (Figure 4). For 1973-74 and 1987-86, the annual-mean correlation
549 was estimated to be about -0.1 and is below the level of statistical significance (Figure 4b).
550 Overall, from 1960 to 2019, there were 19 events that lasted up to 1.8 years in duration when
551 correlations between the SLA and river discharge were statistically insignificant or even negative
552 (Figure 4b). This calls into question the correlations between Churchill River discharge and SLA
553 in Churchill reported by *Gough and Robinson* (2000) and *Gough et al.* (2005). Note that the
554 period from 1972 to 1989 used by *Tushingham* (1992) overlaps with the majority of the period
555 from 1974 to 1994 used by *Gough and Robinson* (2000).

556 Second, *Ward et al.* (2018) analyzed daily data from the Global Runoff Data Centre for 187
557 stations including Churchill and daily maxima sea level data from the Global Extreme Sea-level
558 Analysis. They found no statistically significant dependence between annual maxima of the
559 Churchill River discharge and sea level. For comparison, along the Pacific coast of North
560 America, the correlation ranged from 0.2 to 0.4, and accounted for 4-16% of the variation in sea
561 level. This is consistent with a previous concern about significant impact of Churchill River
562 discharge on SLA in Churchill.

563 Third, our analysis shows that the seasonal cycle in sea level variability with positive SLA
564 during fall is observed not only in Churchill, but also along the eastern coast of Hudson Bay in
565 Innujuaq (Figures 1 and 9). While the sea level record at Innujuaq is short and not continuous,
566 a positive SLA is recognizable during fall 1969-70 and 1973-76 (Figure 9, blue line). Note that
567 the seasonal SLA at Innujuaq cannot be generated locally because the annual mean (1964-2000)
568 discharge of the local Innujuaq River is only $3.3 \text{ km}^3 \text{ year}^{-1}$, about three times smaller than the
569 Churchill River discharge post-diversion (*Godin et al.*, 2017). In contrast, the seasonal pattern in
570 SLA at Innujuaq is generated by the same cyclonic forcing as in Churchill. Seasonal SLA in
571 Innujuaq is consistent with seasonal amplification of atmospheric vorticity (Figures 5b and 9).
572 Moreover, in Innujuaq, the sea level peaks on 18 October and 25 November 1969 are coherent
573 with peaks in atmospheric vorticity (Figure 9) and sea level at Churchill (Figure 6a). From the
574 preceding analysis we explicitly know that these two vorticity peaks were generated by cyclones
575 passing over the Bay (Figure 7a). The coherent peaks in sea level in Churchill and Innujuaq
576 suggest that cyclones that were centered over Hudson Bay on 18 October and 25 November 1969
577 generated storm surge on both the eastern and western coasts of Hudson Bay. This is also
578 supported by a coherent response of sea level to atmospheric forcing at Cape Jones Island and
579 North Kopak Island (Figures 1 and 9). Our hypothesis is also consistent with results of sea level
580 numerical simulations in response to cyclones passing over the Bay in 2016-17 (*Dmitrenko et al.*,
581 2020). For synoptic storm surges, on-shore Ekman transport increases the mass of water column
582 along the coast (the barotropic component). The seasonal baroclinic component appears during
583 summer when water is fresher and warmer causing the thermosteric and halosteric sea-level rise
584 along the coast.

585 Fourth, satellite altimetry reveals a spatially uniform response of sea level to the seasonal cycle
586 in atmospheric vorticity along the whole coast of Hudson Bay (Figure 10). For 1993-2020, we
587 examine the difference between the sea surface heights (SSH) during summer, when monthly
588 mean atmospheric vorticity changes from -0.7 s^{-1} in June to 1.1 s^{-1} in August, and fall, when
589 vorticity increases from 4.2 s^{-1} in September to 7.3 s^{-1} in November (Figure 5b). Results suggest
590 that enhanced cyclonic vorticity during fall generates seasonal SSH elevation over the entire
591 coast of Hudson Bay with SSH differences between fall and summer ranging from $>5 \text{ cm}$ in
592 James Bay to $\sim 1 \text{ cm}$ along the northwest coast (Figure 10). This confirms our results that a
593 positive SLA during fall is generated over the entire coast of Hudson Bay, and particularly in
594 Churchill and Innujuaq, in response to enhanced cyclonic wind forcing (Figures 5a, 5b, and 9).
595 Overall, our third and fourth points suggest that the hypothesis of *Gough and Robinson* (2000)
596 and *Gough et al.* (2005) about a linkage between river discharge into James Bay and SLA in
597 Churchill is inconsistent.

598 One may suggest that seasonal SSH elevation in Figure 10 can be partly due to the thermosteric
599 and halosteric sea-level rise. During summer, the Hudson Bay coastal domain receives large
600 amount of fresh and warm water from river runoff. The seasonal tendency for river discharge,
601 however, is opposite to that for the SSH in Figure 10. For 1988-2000, *Déry et al.* (2005) reported
602 that the total discharge of rivers flowing into Hudson Bay peaks in June at $\sim 3.6 \text{ km}^3 \text{ day}^{-1}$, which
603 significantly exceeds the secondary maximum in October ($\sim 2.3 \text{ km}^3 \text{ day}^{-1}$). The seasonal mean
604 total river discharge in September-November ($\sim 1.9 \text{ km}^3 \text{ day}^{-1}$) is one-and-a-half times smaller
605 compared to $\sim 2.8 \text{ km}^3 \text{ day}^{-1}$ in June-August. Based on these estimates, the river discharge
606 seasonal cycle in June-November is inconsistent with that for the SSH in Figure 10. The
607 cumulative effect of river discharge on the seasonal cycle can play a role, but the residence time
608 of the riverine water fraction in southwestern Hudson Bay during summer is relatively small (~ 1 -
609 3 months; *Granskog et al.*, 2009).

610 Finally, our results on the atmospheric forcing of the Hudson Bay SLA are in agreement with
611 conclusions by *Piecuch and Ponte* (2014, 2015). Using ocean mass measurements from satellite
612 gravimetry conducted during the Gravity Recovery and Climate Experiment, they found that
613 wind forcing dominates sea-level and mass variability in Hudson Bay, and wind might drive
614 Hudson Bay mass changes due to wind-driven outflow through Hudson Strait (*Piecuch and*
615 *Ponte*; 2014). For the sea level interannual variability in Hudson Bay, also evident in Figure 4a,
616 *Piecuch and Ponte* (2015) revealed a wind-driven barotropic fluctuation that explains most of the
617 non-seasonal sea level variance. Furthermore, they suggest that anomalous inflow and outflow
618 through Hudson Strait, which impacts sea level variability in Hudson Bay, are driven by wind
619 stress over Hudson Strait. This highlights the role of wind forcing in amplifying the freshwater
620 outflow from Hudson Bay, as also suggested by *Straneo and Saucier* (2008) and *Dmitrenko et al.*
621 (2020).

622 In summary, we suggest that seasonal amplification of atmospheric vorticity, partially
623 conditioned by the number and strength of cyclones passing over the Bay during fall to early
624 winter, generates the seasonal cycle in sea level variability over the entire Bay as depicted
625 schematically in Figure 11. Cyclones passing over Hudson Bay during fall to early winter cause
626 on-shore Ekman transport and storm surges over the entire coast of Hudson Bay (Figure 11a). In
627 summer, anticyclonic wind forces off-shore Ekman transport lowering sea level along the coastline
628 of Hudson Bay (Figure 11b).

629

630 **Summary and conclusions**

631 Our analysis revealed that in contrast to previous research, the local Churchill River discharge
632 explains only up to 5% of the sea level variability at Churchill. Cyclonic atmospheric forcing is
633 shown to explain from 22% during the ice-covered winter-spring season to 30% during the ice-
634 free summer-fall season (Tables 1-3). Multiple regression analysis showed that atmospheric
635 forcing and local river discharge together can explain up to 32% of the sea level variability at
636 Churchill. We found that a positive sea level anomaly in Churchill during fall is partially
637 conditioned by the seasonal cycle in atmospheric vorticity, with prevailing cyclonic wind forcing

638 during fall to the beginning of winter (Figure 5). Sea-ice cover reduces wind stress on the water
639 column during the ice-covered season from December to May, and cyclonic wind forcing
640 generates positive sea level anomalies at Churchill when only the monthly mean vorticity
641 exceeds $\sim 6\text{-}8\text{ s}^{-1}$ (Figure 8). In this context, transition towards a longer open water season (e.g.,
642 *Hochheim and Barber, 2014*) is expected to increase the contribution of atmospheric forcing to
643 sea level variability.

644 We expanded our observations at Churchill to the bay-wide scale using sea level observations
645 along the eastern coast of the Bay and satellite altimetry. A coherent sea level response to
646 atmospheric forcing observed at the opposite sides of Hudson Bay suggests that the spatial scale
647 of cyclones passing over Hudson Bay roughly equals the Hudson Bay area (Figures 7 and 9, and
648 *Dmitrenko et al., 2020*). This scaling equivalency implies that cyclones passing over Hudson Bay
649 cause on-shore Ekman transport and storm surges over the entire Hudson Bay coast (Figure 11a).
650 This is also consistent with results by *Dmitrenko et al. (2020)* obtained for 2016-17. Moreover,
651 the satellite altimetry data shows that this scaling equivalency works not only for synoptic, but
652 also for the seasonal time scale. The seasonal cycle in atmospheric vorticity (Figure 5b) partially
653 conditions the seasonal cycle in sea level variability over the entire coast of Hudson Bay. The
654 recurring cyclonic wind forcing during fall favors sea level elevation over the entire Hudson Bay
655 coast compared to summer (Figures 10 and 11). This seasonal pattern in sea-level variability
656 seems to have implication for geostrophic circulation. The cross-shelf pressure gradient
657 generated due to seasonal amplification of sea level along the coast drives alongshore
658 geostrophic flow and favors the cyclonic circulation around Hudson Bay during fall to earlier
659 winter. In contrast, during summer the geostrophic component attributed to the anticyclonic
660 atmospheric forcing disrupts the Hudson Bay cyclonic circulation as shown by *Ridenour et al.*
661 (2019a).

662 Our research is important for maritime activity within the Bay. Communities around the Bay rely
663 heavily on the annual summer sea-lift to re-supply them at a fraction of the price compared to air
664 transport (*Kuzyk and Candlish, 2019*). In this context, positive coastal sea level anomalies during
665 fall favor re-supply operations to coastal communities. However, increased cyclonic activity
666 during fall is also associated with extreme wind events (Figure 2b) and storm surges (e.g., Figure
667 6) increasing risks to re-supply and fuel-transfer operations.

668 The origin of seasonality in wind forcing, its climatic aspects and ocean response to seasonal and
669 interannual variability in atmospheric vorticity over the Bay are among important priorities for
670 our future research. The freshwater storage in Hudson Bay and export through Hudson Strait
671 seem to be directly impacted by seasonal and interannual variability in wind forcing, clearly
672 defining the need for further research in this area using multi-year numerical simulations and
673 atmospheric reanalyses. Seasonality of the wind forcing is the hypothesized cause of the sea
674 level variability, but probably does not provide a complete explanation. The steric changes in
675 coastal zone attributed to river runoff were not taken into account that points out a necessity for
676 future research involving numerical simulations. Possible impacts of climate change on cyclone
677 activity in Hudson Bay, and therefore sea-level variability, will be addressed in future research.

678

679 **Data availability**

680 Sea level data used in this study are available from the Canadian Tides and Water Levels Data
681 Archive of the Fisheries and Oceans Canada through [http://www.isdm-gdsi.gc.ca/isdm-gdsi/twl-](http://www.isdm-gdsi.gc.ca/isdm-gdsi/twl-mne/index-eng.htm#s5)
682 [mne/index-eng.htm#s5](http://www.isdm-gdsi.gc.ca/isdm-gdsi/twl-mne/index-eng.htm#s5) (last access: 26 August 2021). The daily SLA/ADT maps with all
683 corrections applied are distributed via CMEMS (<https://marine.copernicus.eu/>; last access: 26
684 August 2021). Churchill River discharge data are provided in supplementary material. SLP and
685 wind data are available from the <https://psl.noaa.gov/data/composites/hour/> and
686 <https://psl.noaa.gov/cgi-bin/data/testdap/timeseries.pl> (last access: 26 August 2021).

687

688 **Author contributions**

689 Conceptualization: ID; methodology: ID, DV, TS, AT; formal analysis: ID, DV, AT;
690 investigation: ID, DV, AC, TS; resources: KS, DBarber; data curation: ID, DV, AT; writing
691 (original draft): ID, DV, TS; writing (review & editing): AC, DV, SK, TS, AT, DBabb;
692 visualization: ID, DV; supervision: DBarber; project administration: KS, DBarber; funding
693 acquisition: KS, DBarber.

694

695 **Competing interests**

696 The authors declare that they have no conflict of interest.

697

698 **Acknowledgments**

699 This work is a part of research conducted under the framework of the Arctic Science Partnership
700 (ASP) and ArcticNet. This research is also a contribution to the Natural Sciences and
701 Engineering Council of Canada (NSERC) Collaborative Research and Development project:
702 BaySys (CRDPJ470028-14). Funding for this work was provided by NSERC, Manitoba Hydro,
703 the Canada Excellence Research Chair (CERC) program, the Canada Research Chairs (CRC)
704 program and the Canada-150 Research Chairs program. D. Babb is additionally supported by
705 NSERC and the Canadian Meteorological and Oceanographic Society (CMOS). DLV was
706 supported by NOAA Atlantic Oceanographic and Meteorological Laboratory under the auspices
707 of the Cooperative Institute for Marine and Atmospheric Studies (CIMAS), a cooperative
708 institute of the University of Miami and NOAA, cooperative agreement NA20OAR4320472.

709

710

711 **References**

712 Andrews, J., Babb, D., and Barber, D. G.: Climate change and sea ice: Shipping accessibility on
713 the marine transportation corridor through Hudson Bay and Hudson Strait (1980 –2014), *Elem.*
714 *Sci. Anth.*, 5, 15, <https://doi.org/10.1525/elementa.13>, 2017.

- 715 CLS-DOS: Validation of altimeter data by comparison with tide gauge measurements: yearly
716 report 2016, Ref. CLS-DOS-17-0016, available at:
717 [https://www.aviso.altimetry.fr/fileadmin/documents/calval/validation_report/annual_report_TG_](https://www.aviso.altimetry.fr/fileadmin/documents/calval/validation_report/annual_report_TG_2016.pdf)
718 2016.pdf, 2016, last access: 26 August 2021.
- 719 Copernicus Climate Change Service (C3S): ERA5: Fifth generation of ECMWF atmospheric
720 reanalyses of the global climate. Copernicus Climate Change Service Climate Data Store (CDS),
721 2017, available at <https://cds.climate.copernicus.eu/cdsapp#!/home>, last access: 26 August 2021.
- 722 Déry, S. J., Stieglitz, M., McKenna, E. C., and Wood, E. F.: Characteristics and trends of river
723 discharge into Hudson, James, and Ungava Bays, 1964–2000, *J. Climate*, 18, 2540–2557,
724 <https://doi.org/10.1175/JCLI3440.1>, 2005.
- 725 Déry, S. J., Mlynowski, T. J., Hernández-Henríquez, M. A., and Straneo, F.: Interannual
726 Variability and Interdecadal Trends in Hudson Bay Streamflow, *Journal of Marine Systems*, 88
727 (3), 341–351, <https://doi.org/10.1016/j.jmarsys.2010.12.002>, 2011.
- 728 Déry, S. J., Stadnyk, T. A., MacDonald, M. K., and Gaudi-Sharma, B.: Recent trends and
729 variability in river discharge across northern Canada, *Hydrology and Earth System Sciences*, 20,
730 4801–4818, <https://doi.org/10.5194/hess-20-4801-2016>, 2016.
- 731 Dmitrenko, I. A., Kirillov, S. A., and Tremblay, L. B.: The long-term and interannual variability
732 of summer fresh water storage over the eastern Siberian shelf: Implication for climatic change, *J.*
733 *Geophys. Res.*, 113, C03007, <https://doi.org/10.1029/2007JC004304>, 2008a.
- 734 Dmitrenko, I. A., Kirillov, S. A., Tremblay, L. B., Bauch, D., and Makhotin, M.: Effects of
735 atmospheric vorticity on the seasonal hydrographic cycle over the eastern Siberian shelf,
736 *Geophys. Res. Lett.*, 35, L03619, <https://doi.org/10.1029/2007GL032739>, 2008b.
- 737 Dmitrenko, I. A., Myers, P. G., Kirillov, S. A., Babb, D. G., Volkov, D. L., Lukovich, J. V., Tao,
738 R., Ehn, J. K., Sydor, K., and Barber, D. G.: Atmospheric vorticity sets the basin-scale
739 circulation in Hudson Bay, *Elem. Sci. Anth.*, 8, 49, <https://doi.org/10.1525/elementa.049>, 2020.
- 740 Dmitrenko, I. A., Kirillov, S. A., Babb, D. G., Kuzyk, Z. A., Basu, A., Ehn, J. K., Sydor, K., and
741 Barber D. G.: Storm-driven hydrography of western Hudson Bay, *Continental Shelf Res.*, 227,
742 104525, <https://doi.org/10.1016/j.csr.2021.104525>, 2021.
- 743 Eastwood, R. A., McDonald, R., Ehn, J., Heath, J., Arragutainaq, L., Myers, P. G., Barber, D.,
744 and Kuzyk, Z. A.: Role of river runoff and sea-ice brine rejection in controlling stratification
745 throughout winter in southeast Hudson Bay, *Estuaries and Coasts*, 43, 756–786,
746 <https://doi.org/10.1007/s12237-020-00698-0>, 2020.
- 747 Fisher, R. A.: On the 'probable error' of a coefficient of correlation deduced from a small sample,
748 *Metron*, 1, 3–32, 1921.
- 749 Foreman, M. G. G.: Manual for tidal heights analysis and prediction, Pacific Marine Science
750 Report, 77–10, Patricia Bay, Sidney, BC, Institute of Ocean Sciences, 58 pp., 1977.

- 751 Godin, P., Macdonald, R. W., Kuzyk, Z. Z. A., Goñi, M. A., and Stern, G. A.: Organic matter
752 compositions of rivers draining into Hudson Bay: Present-day trends and potential as recorders
753 of future climate change, *J. Geophys. Res. Biogeosci.*, 122, 1848–1869,
754 <https://doi.org/10.1002/2016JG003569>, 2017.
- 755 Gough, W. A.: Projections of sea-level change in Hudson and James Bays, Canada, due to global
756 warming, *Arctic and Alpine Research*, 30(1), 84–88, <https://doi.org/10.2307/1551748>, 1998.
- 757 Gough, W. A., and Robinson, C. A.: Sea-level Variation in Hudson Bay, Canada, from Tide-
758 Gauge Data, *Arctic, Antarctic, and Alpine Research*, 32(3), 331–335,
759 <https://doi.org/10.1080/15230430.2000.12003371>, 2000.
- 760 Gough, W. A., Robinson, C., and Hosseinian, R.: The Influence of James Bay River Discharge
761 on Churchill, Manitoba Sea Level, *Polar Geography*, 29(5), 213–223,
762 <https://doi.org/10.1080/789610202>, 2005.
- 763 Granskog, M. A., Macdonald, R. W., Kuzyk, Z. A., Senneville, S., Mundy, C.-J., Barber, D. G.,
764 Stern, G. A., and Saucier, F.: Coastal conduit in southwestern Hudson Bay (Canada) in summer:
765 Rapid transit of freshwater and significant loss of colored dissolved organic matter, *J. Geophys.*
766 *Res.*, 114, C08012, <https://doi.org/10.1029/2009JC005270>, 2009.
- 767 Granskog, M. A., Kuzyk, Z. A., Azetsu-Scott, K., and Macdonald, R. W.: Distributions of
768 runoff, sea-ice melt and brine using $\delta^{18}\text{O}$ and salinity data - A new view on freshwater cycling
769 in Hudson Bay, *Journal of Marine Systems*, 88, 362–374,
770 <https://doi.org/10.1016/j.jmarsys.2011.03.011>, 2011.
- 771 Guttenberg, B.: Changes in sea level, postglacial uplift, and mobility of the earth's interior,
772 *Geological Society of America Bulletin*, 52(5), 721–772, <https://doi.org/10.1130/GSAB-52-721>,
773 1941.
- 774 Hersbach, H., and Coauthors: The ERA5 global reanalysis, *Quarterly Journal of the Royal*
775 *Meteorological Society*, 146, 1999–2049, <https://doi.org/10.1002/qj.3803>, 2020.
- 776 Hochheim, K. P., and Barber, D. G.: Atmospheric forcing of sea ice in Hudson Bay during the
777 fall period, 1980–2005. *J. Geophys. Res.*, 115, C05009, <https://doi.org/10.1029/2009JC005334>,
778 2010.
- 779 Hochheim, K. P., and Barber, D. G.: An update on the ice climatology of the Hudson Bay
780 System. *Arctic Antarctic Alpine Res.*, 46(1), 66–83, <https://doi.org/10.1657/1938-4246-46.1.66>,
781 2014.
- 782 Ingram, R. G. and Prinsenberg, S.: Coastal oceanography of Hudson Bay and surrounding
783 Eastern Canadian Arctic Waters, In: Robinson, A. R. and K. N. Brink (Eds.), *The Sea*, Vol. 11.
784 The Global Coastal Ocean Regional Studies and Synthesis. Harvard University Press,
785 Cambridge, Massachusetts and London, 835–861, 1998.
- 786 Joyce, B. R., Pringle, W. J., Wirasaet, D., Westerink, J. J., Van der Westhuysen, A. J., Grumbine,
787 R., and Feyen, J.: High resolution modeling of western Alaskan tides and storm surge under

- 788 varying sea ice conditions, *Ocean Modelling*, 141, 101421,
789 <https://doi.org/10.1016/j.ocemod.2019.101421>, 2019.
- 790 Kalnay, E., Kanamitsu, M., Kistler, R., Collins, W., Deaven, D., Gandin, L., Iredell, M., Saha, S.,
791 White, G., Woollen, J., Zhu, Y., Chelliah, M., Ebisuzaki, W., Higgins, W., Janowiak, J., Mo, K.
792 C., Ropelewski, C., Wang, J., Leetmaa, A., Reynolds, R., Jenne, R., and Joseph D.: The
793 NCEP/NCAR 40-year reanalysis project, *Bull. Am. Meteorol. Soc.*, 77, 437–471,
794 [https://doi.org/10.1175/1520-0477\(1996\)077<0437: TNYRP>2.0.CO;2](https://doi.org/10.1175/1520-0477(1996)077<0437: TNYRP>2.0.CO;2), 1996.
- 795 Kuzyk, Z. A., Macdonald, R.W., Stern, G. A., and Gobeil, C.: Inferences about the modern
796 organic carbon cycle from diagenesis of redox-sensitive elements in Hudson Bay, *Journal of*
797 *Marine Systems*, 88, 451–462, <https://doi.org/10.1016/j.jmarsys.2010.11.001>, 2011.
- 798 Kuzyk, Z. A. and Candlish, L. M.: From Science to Policy in the Greater Hudson Bay Marine
799 Region: An Integrated Regional Impact Study (IRIS) of Climate Change and Modernization,
800 ArcticNet, Québec City, 424 pp, 2019
- 801 Landy, J. C., Ehn, J. K., Babb, D. G., Theriault, N., and Barber D. G.: Sea ice thickness in the
802 eastern Canadian Arctic: Hudson Bay complex & Baffin Bay, *Remote Sensing of Environment*,
803 200, 281–294, <https://doi.org/10.1016/j.rse.2017.08.019>, 2017.
- 804 Larson, K. M., and van Dam, T.: Measuring postglacial rebound with GPS and absolute gravity,
805 *Geophys. Res. Lett.*, 27, 3925–3928, <https://doi.org/10.1029/2000GL011946>, 2000.
- 806 Lüpkes, C., Gryanik, V. M., Hartmann, J., and Andreas, E. L.: A parametrization, based on sea
807 ice morphology, of the neutral atmospheric drag coefficients for weather prediction and climate
808 models, *J. Geophys. Res. Atmospheres*, 117, D13112, <https://doi.org/10.1029/2012JD017630>,
809 2012.
- 810 Mulet, S., Rio, M. H., Greiner, E., Picot, N., and Pascual, A.: New global Mean Dynamic
811 Topography from a GOCE geoid model, altimeter measurements and oceanographic in-situ data,
812 OSTST Boulder, USA, available at:
813 http://www.aviso.altimetry.fr/fileadmin/documents/OSTST/2013/oral/mulet_MDT_CNES_CLS
814 13.pdf, 2013, last access: 26 August 2021.
- 815 Pascual, A., Boone, C., Larnicol, G., and Le Traon, P.-Y.: On the quality of real-time altimeter
816 gridded fields: Comparison with in situ data, *J. Atmos. Oceanic Technol.*, 26, 556–569,
817 <https://doi.org/10.1175/2008JTECHO556.1>, 2009.
- 818 Piecuch, C. G., and Ponte, R. M.: A wind-driven nonseasonal barotropic fluctuation of the
819 Canadian inland seas, *Ocean Sci.*, 11, 175–185, <https://doi.org/10.5194/os-11-175-2015>, 2015.
- 820 Piecuch, C. G., and Ponte, R. M.: Nonseasonal mass fluctuations in the midlatitude North
821 Atlantic Ocean, *Geophys. Res. Lett.*, 41, 4261–4269, <https://doi.org/10.1002/2014GL060248>,
822 2014.
- 823 Prinsenber, S. J.: Freshwater contents and heat budgets of James Bay and Hudson Bay,
824 *Continental Shelf Res.*, 3(2), 191-200, [https://doi.org/10.1016/0278-4343\(84\)90007-4](https://doi.org/10.1016/0278-4343(84)90007-4), 1984.

- 825 Prinsenberg, S. J.: Salinity and temperature distribution of Hudson Bay and James Bay, In:
826 Martini, E. P. (ed.) Canadian Inland Seas, Oceanogr. Ser. 44, Elsevier, New York, pp 163–186,
827 1986a.
- 828 Prinsenberg, S. J.: The circulation pattern and current structure of Hudson. In: Martini, E. P. (ed.)
829 Canadian Inland Seas, Oceanogr. Ser. 44, Elsevier, New York, 187–203, 1986b.
- 830 Prinsenberg, S. J.: Ice-cover and ice-ridge contributions to the freshwater contents of Hudson
831 Bay and Foxe Basin, Arctic, 41(1), 6–11, <https://doi.org/10.14430/arctic1686>, 1988.
- 832 Prinsenberg, S. J.: Effects of hydro-electric projects on Hudson Bay's marine and ice
833 environments, Potential Environ. Impacts Ser. 2, 8 pp., North Wind Inf. Serv., Montreal, 1991.
- 834 Pujol, M.-I., Faugère, Y., Taburet, G., Dupuy, S., Pelloquin, C., Ablain, M., and Picot, N.:
835 DUACS DT2014: the new multi-mission altimeter data set reprocessed over 20 years, Ocean
836 Sci., 12, 1067-1090, <https://doi.org/0.5194/os-12-1067-2016>, 2016.
- 837 Pew Charitable Trusts: The Integrated Arctic Corridors Framework. Planning for responsible
838 shipping in Canada's Arctic waters, available at:
839 [https://www.pewtrusts.org/~media/Assets/2016/04/The-Integrated-Arctic-Corridors-](https://www.pewtrusts.org/~media/Assets/2016/04/The-Integrated-Arctic-Corridors-Framework.pdf)
840 [Framework.pdf](https://www.pewtrusts.org/~media/Assets/2016/04/The-Integrated-Arctic-Corridors-Framework.pdf), 2016, last access: 26 August 2021.
- 841 Ray, R. D.: Sea Level, Land Motion, and the Anomalous Tide at Churchill, Hudson Bay,
842 American Geophysical Union, Fall Meeting 2015, abstract id. G43B-1040, 2015.
- 843 Ridenour, N. A., Hu, X., Sydor, K., Myers, P. G., and Barber, D. G.: Revisiting the circulation of
844 Hudson Bay: Evidence for a seasonal pattern, Geophysical Research Letters, 46, 3891–3899,
845 <https://doi.org/10.1029/2019GL082344>, 2019a.
- 846 Ridenour, N. A., Hu, X., Jafarikhasragh, S., Landy, J. C., Lukovich, J. V., Stadnyk, T. A., Sydor,
847 K., Myers, P. G., and Barber, D. G.: Sensitivity of freshwater dynamics to ocean model
848 resolution and river discharge forcing in the Hudson Bay Complex, Journal of Marine Systems,
849 196, 48-64, <https://doi.org/10.1016/j.jmarsys.2019.04.002>, 2019b.
- 850 Sella, G. F., Stein, S., Dixon, T. H., Craymer, M., James, T. S., Mazzotti, S., and Dokka, R. K.:
851 Observation of glacial isostatic adjustment in “stable” North America with GPS, Geophys. Res.
852 Lett., 34, L02306, <https://doi.org/10.1029/2006GL027081>, 2007.
- 853 Smith, C. A., Compo, G. P., and Hooper, D. K.: Web-based reanalysis intercomparison tools
854 (WRIT) for analysis and comparison of reanalyses and other datasets, Bull. Amer. Meteor. Soc.,
855 95(11): 1671–1678, <https://doi.org/10.1175/BAMS-D-13-00192.1>, 2014.
- 856 Saucier, F. J., and Dionne, J.: A 3-D coupled ice-ocean model applied to Hudson Bay, Canada:
857 The seasonal cycle and time-dependent climate response to atmospheric forcing and runoff, J.
858 Geophys. Res. Oceans, 103(C12), 27,689-27,705, <https://doi.org/10.1029/98JC02066>, 1998.
- 859 Saucier, F. J., Senneville, S., Prinsenberg, S., Roy, F., Smith, G., Gachon, P., Caya, D., and
860 Laprise, R.: Modelling the sea ice-ocean seasonal cycle in Hudson Bay, Foxe Basin and Hudson

- 861 Strait, Canada, *Climate Dynamics*, 23, 303–326, <https://doi.org/10.1007/s00382-004-0445-6>,
862 2004.
- 863 Schulze, L. M, and Pickart, R. S.: Seasonal variation of upwelling in the Alaskan Beaufort Sea:
864 Impact of sea ice cover, *J. Geophys. Res.*, 117, C06022, <https://doi.org/10.1029/2012JC007985>,
865 2012.
- 866 St-Laurent, P., Straneo, F., Dumais, J.-F., and Barber, D. G.: What is the fate of the river waters
867 of Hudson Bay?, *Journal of Marine Systems*, 88, 352–361,
868 <https://doi.org/10.1016/j.jmarsys.2011.02.004>, 2011.
- 869 Straneo, F., and Saucier, F.: The outflow from Hudson Strait and its contribution to the Labrador
870 Current, *Deep-Sea Res. I*, 55, 926– 946, <https://doi.org/10.1016/j.dsr.2008.03.012>, 2008.
- 871 The Climate Change Initiative Coastal Sea Level Team. Coastal sea level anomalies and
872 associated trends from Jason satellite altimetry over 2002–2018: *Sci. Data*, 7, 357,
873 <https://doi.org/10.1038/s41597-020-00694-w>, 2020.
- 874 Tivy, A., Howell, S. E., Alt, B., Yackel, J. J., and Carrieres, T.: Origins and levels of seasonal
875 forecast skill for sea ice in Hudson Bay using Canonical Correlation Analysis, *J. Climate*, 24(5),
876 1378-1395, <https://doi.org/10.1175/2010JCLI3527.1>, 2011.
- 877 Tsamados, M., Feltham, D. L., Schroeder, D., Flocco, D., Farrell, S. L., Kurtz, N., Laxon, S. W.,
878 and Bacon, S.: Impact of Variable Atmospheric and Oceanic Form Drag on Simulations of
879 Arctic Sea Ice, *J. Phys. Oceanography*, 44(5), 1329–1353, <https://doi.org/10.1175/JPO-D-13-0215.1>, 2014.
- 881 Tushingham, A. M.: Observations of postglacial uplift at Churchill, Manitoba, *Canadian Journal*
882 *of Earth Sciences*, 29, 2418-2425, <https://doi.org/10.1139/e92-189>, 1992.
- 883 Volkov, D. L., and Pujol, M.-I.: Quality assessment of a satellite altimetry data product in the
884 Nordic, Barents, and Kara seas, *J. Geophys. Res.*, 117, C03025,
885 <https://doi.org/10.1029/2011JC007557>, 2012.
- 886 Volkov, D. L., Larnicol, G., and Dorandeu, J.: Improving the quality of satellite altimetry data
887 over continental shelves, *J. Geophys. Res.*, 112, C06020, <https://doi.org/10.1029/2006JC003765>,
888 2007.
- 889 Ward, P. J., Couasnon, A., Eilander, D., Haigh, I. D., Hendry, A., Muis, S., Veldkamp, T. I. E.,
890 Winsemius, H. C., and Wahl, T.: Dependence between high sea-level and high river discharge
891 increases flood hazard in global deltas and estuaries, *Environ. Res. Lett.*, 13, 084012,
892 <https://doi.org/10.1088/1748-9326/aad400>, 2018.
- 893 Walsh, J. E., Chapman, W. L., and Shy, T. L.: Recent decrease of sea level pressure in the
894 central Arctic, *J. Clim.*, 9, 480–486, [https://doi.org/10.1175/1520-0442\(1996\)009<0480:
895 RDOSLP>2.0.CO;2](https://doi.org/10.1175/1520-0442(1996)009<0480:RDOSLP>2.0.CO;2), 1996.
- 896 Wang, J., L. Mysak, A. and Ingram, R. G.: A Three-Dimensional Numerical Simulation of
897 Hudson Bay Summer Ocean Circulation: Topographic Gyres, Separations, and Coastal Jets, *J.*

898 Phys. Oceanogr., 24, 2496–2514, <https://doi.org/10.1175/1520->
899 0485(1994)024<2496:ATDNSO>2.0.CO;2, 1994.

900 Wolf, D., Klemann, V. and Wunsch, J.: A Reanalysis and Reinterpretation of Geodetic and
901 Geological Evidence of Glacial-Isostatic Adjustment in the Churchill Region, Hudson Bay, Surv.
902 Geophys., 27, 19–61, <https://doi.org/0.1007/s10712-005-0641-x>, 2006.

903 **Tables**

904 **Table 1:** Correlations (R) of daily atmospheric vorticity and/or Churchill River discharge against
 905 sea level anomalies in western Hudson Bay for the whole annual cycle

Predictor(s)/Time frame	1960 - 2019	Pre-diversion 1960 - 1976	Post-diversion 1977 - 2019
Vorticity	0.47	0.49	0.47
River discharge	0.22	0.20	0.23
Vorticity and river discharge*	0.53*	0.53*	0.53*

906

907 **Table 2:** Correlations (R) of monthly-mean atmospheric vorticity and/or Churchill River
 908 discharge against sea level anomalies in western Hudson Bay for the ice-free period (June-
 909 November)

Predictor(s)/Time frame	1960 - 2019	Pre-diversion 1960 - 1976	Post-diversion 1977 - 2019
Vorticity	0.54	0.52	0.55
River discharge	0.08	0.03**	0.11
Vorticity and river discharge*	0.55*	0.52*	0.57*

910

911 **Table 3:** Correlations (R) of monthly-mean atmospheric vorticity and/or Churchill River
 912 discharge against sea level anomalies in western Hudson Bay for the ice-covered period
 913 (December-May)

Predictor(s)/Time frame	1960 - 2019	Pre-diversion 1960 - 1976	Post-diversion 1977 - 2019
Vorticity	0.47	0.49	0.47
River discharge	0.21	0.12	0.19
Vorticity and river discharge*	0.52*	0.51*	0.52*

914

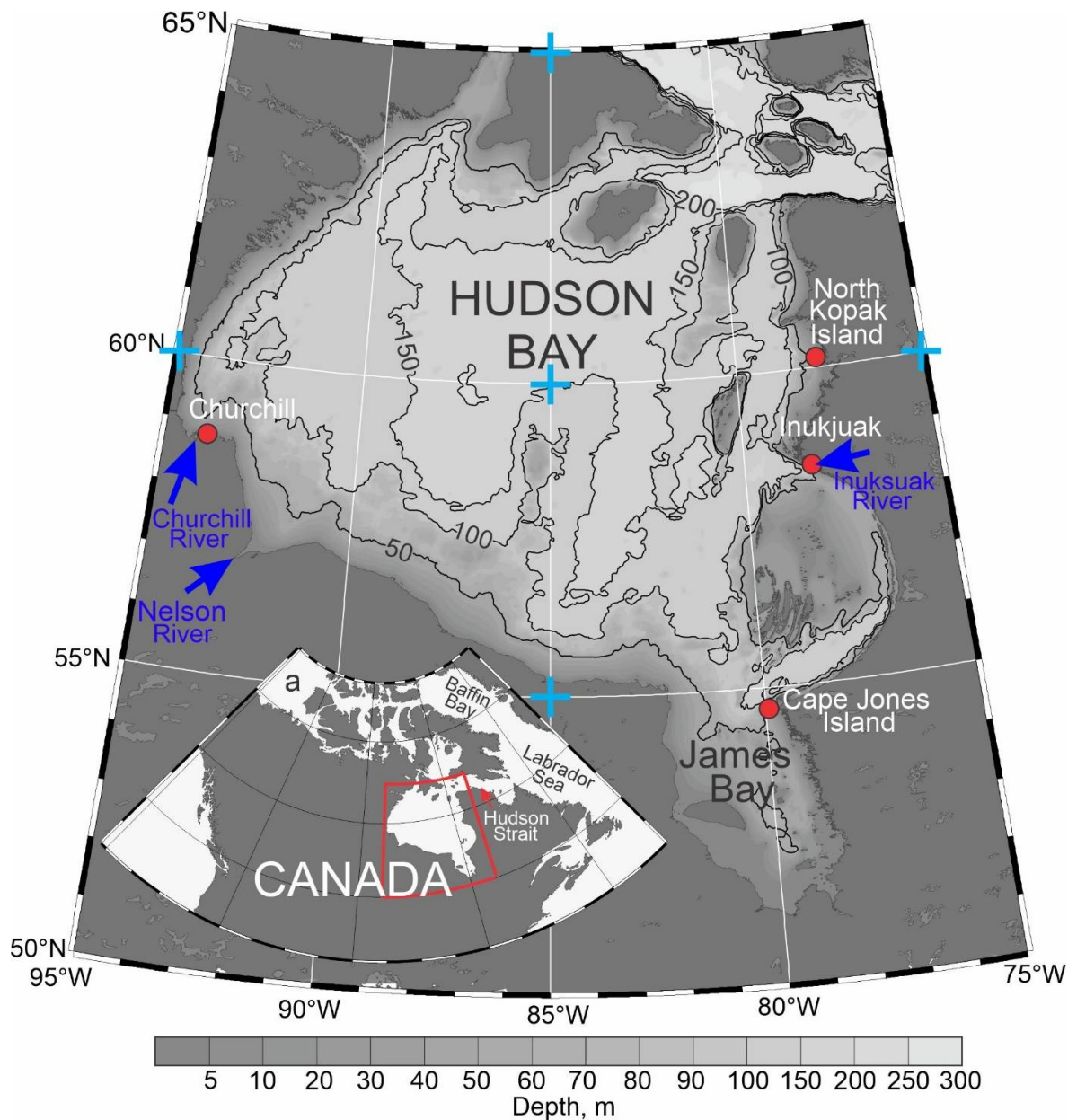
915 *The coefficient of multiple correlation is estimated based on the multiple linear regression
 916 analysis

917 ** Correlation not statistically significant at the 99% confidence level

918 **Figures**

919

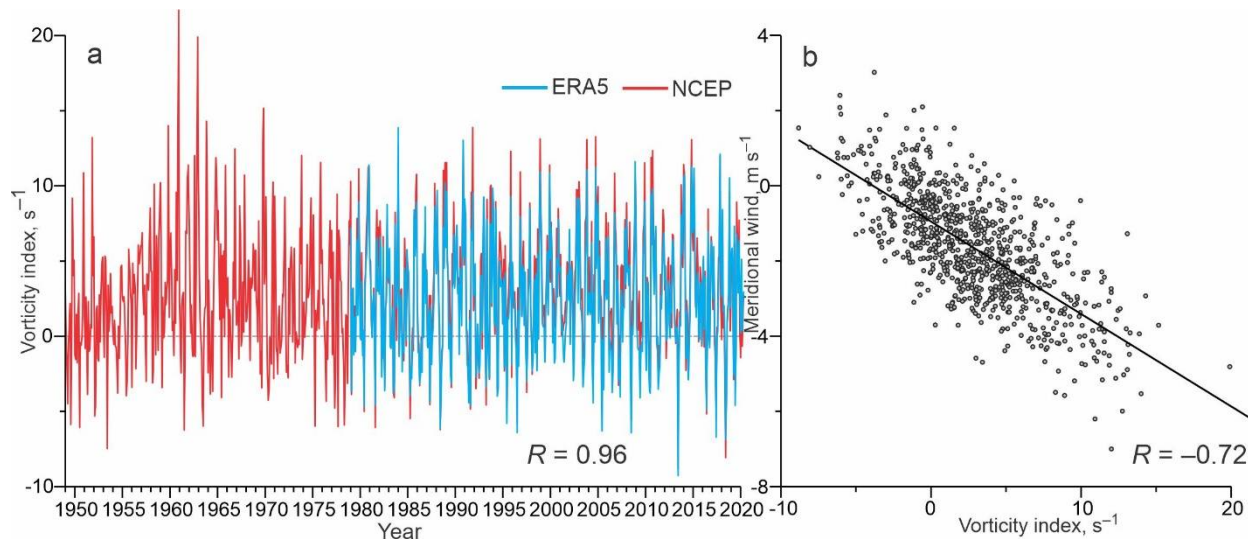
920



921

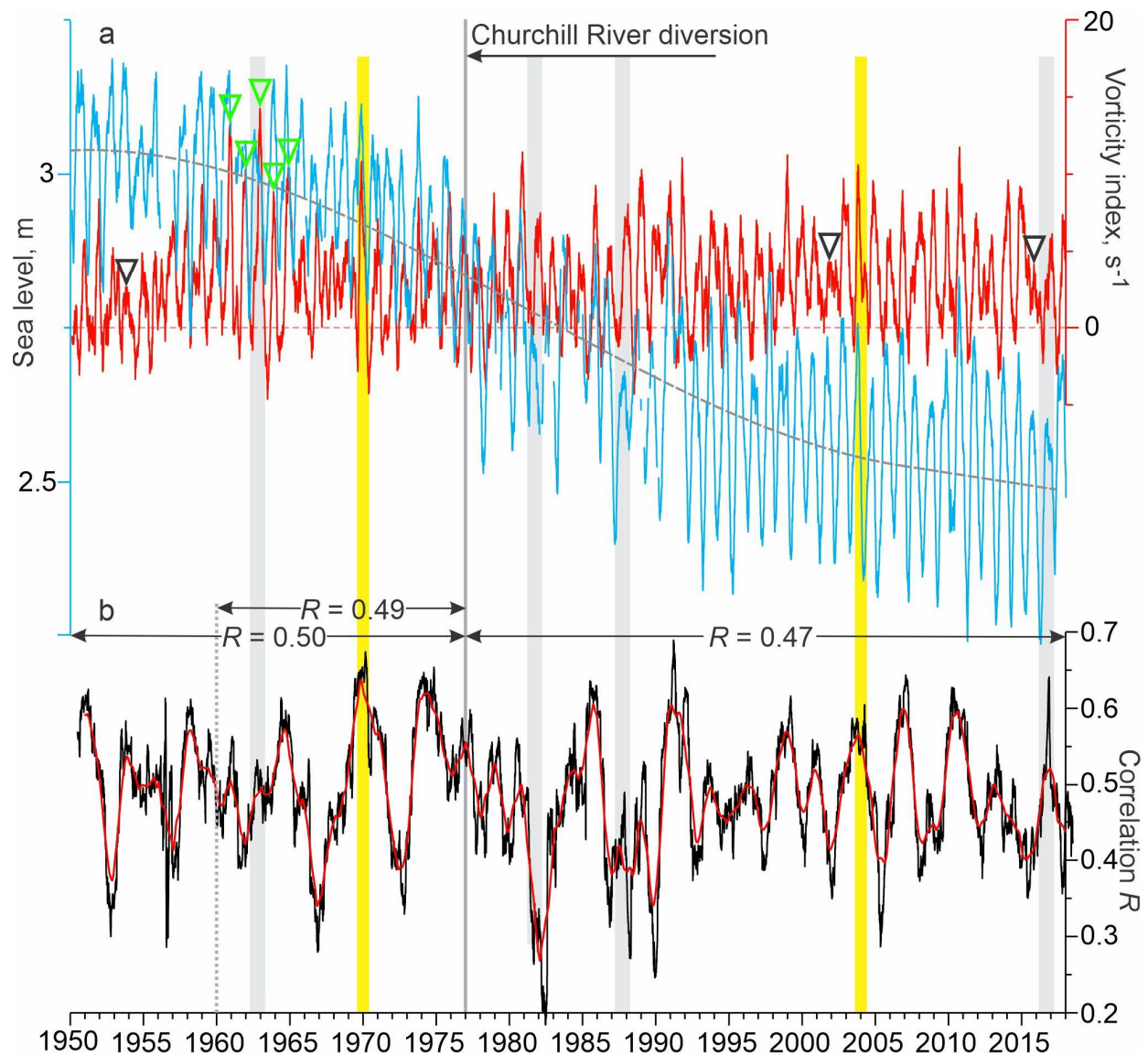
922 **Figure 1:** Map of Hudson Bay. Red dots depict the permanent tide gauge in Churchill and
 923 temporary tide gauges in Inukjuak, Cape Jones Island and North Kopak Island. Blue arrows
 924 highlight Churchill, Nelson and Inuksuak river mouths. Blue crosses depict the 5-point stencil
 925 used for computing atmospheric vorticity approximated as Laplacian from sea level atmospheric
 926 pressure. The numbered black lines depict depth contours of 50, 100, 150 and 200 m. (a) Inset
 927 shows the Hudson Bay location within North America. The map of Hudson Bay was compiled
 928 based on the General Bathymetric Chart of the Oceans (GEBCO, www.gebco.net).

929
930
931
932
933
934



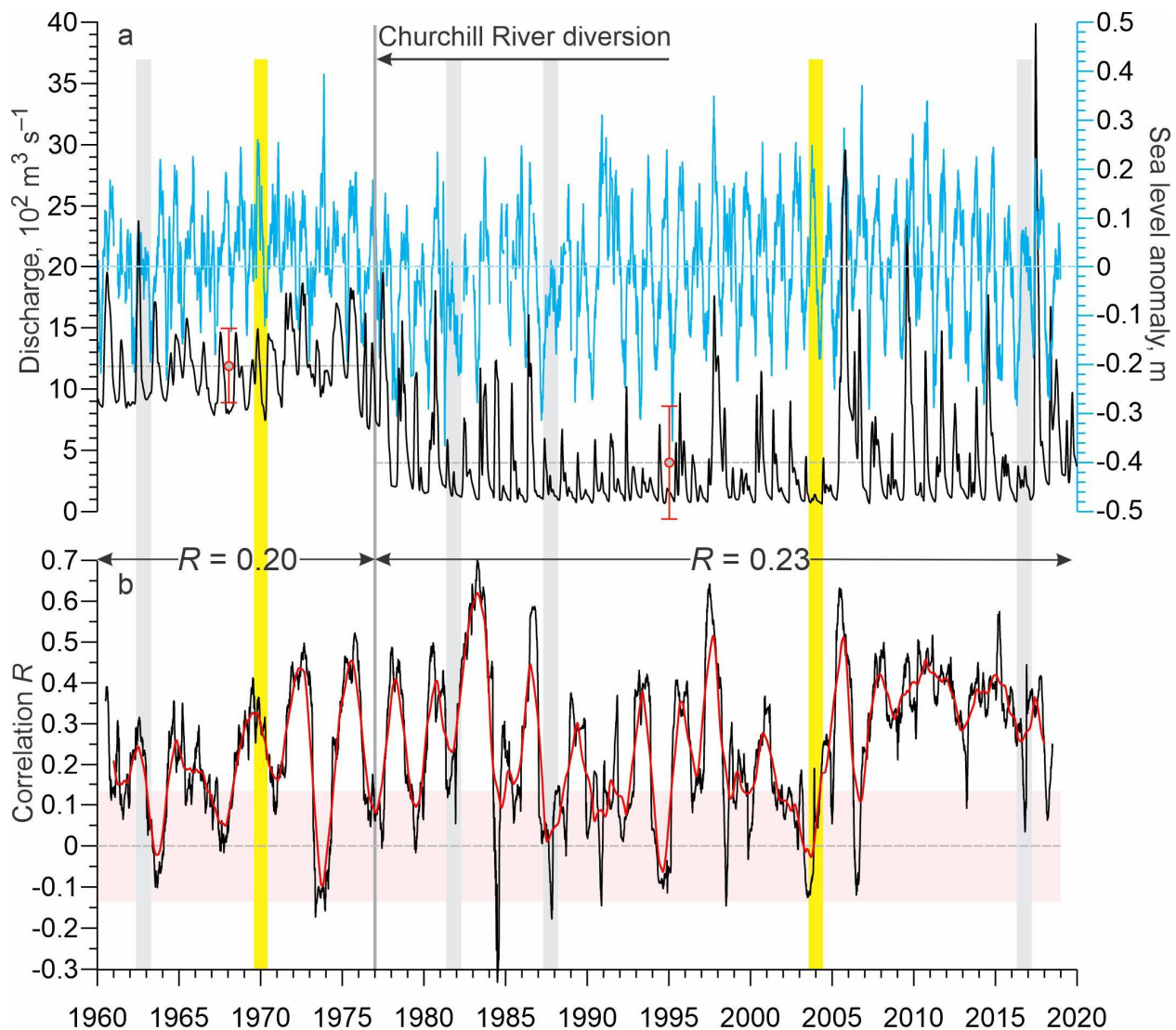
935
936
937
938
939
940
941
942
943

Figure 2: (a) Time series of the monthly mean atmospheric vorticity index (s^{-1}) over Hudson Bay, derived from NCEP (red) and ERA5 (blue). (b) Scatter plot of the monthly mean meridional wind seaward of Churchill in western Hudson Bay ($m s^{-1}$) versus the monthly mean atmospheric vorticity index. Thick black line depicts linear regression. Numbers at the bottom show correlation R between (a) the monthly mean vorticity derived from NCEP (1949-2000) and ERA5 (1979-2000) and (b) the monthly mean NCEP vorticity versus meridional wind (1949-2020).



944
 945 **Figure 3:** (a) 91-day running mean of daily mean atmospheric vorticity index (red, s⁻¹) over
 946 Hudson Bay and sea level measured at the tide gauge in Churchill (blue, m). Positive and
 947 negative vorticity correspond to cyclonic and anticyclonic atmospheric circulation, respectively.
 948 Gray dashed line shows polynomial approximation of the sea level trend attributed to the glacial
 949 isostatic adjustment. Black and green triangles show periods when seasonal vorticity from late
 950 fall to early winter was diminished and amplified, respectively. (b) Correlation R between daily
 951 vorticity index and sea level anomaly (SLA) computed for the 365-day moving window (black)
 952 with their 365-day running mean (red). All correlations are statistically significant at 99%
 953 confidence. Numbers at the top show correlation between daily vorticity index and SLA
 954 computed for 1950/60-1976 and 1977-2018 pre- and post-diversion, respectively. (a, b) Yellow
 955 shading highlights August-May 1969-70 and 2003-04, enlarged in Figure 6. Black arrow
 956 indicates onset of the Churchill River diversion. Gray shading highlights periods when the sea
 957 level seasonal cycle was partially disrupted (1981-82 and 1987-88), or significantly diminished
 958 (1962-63 and 2016-2017).

959

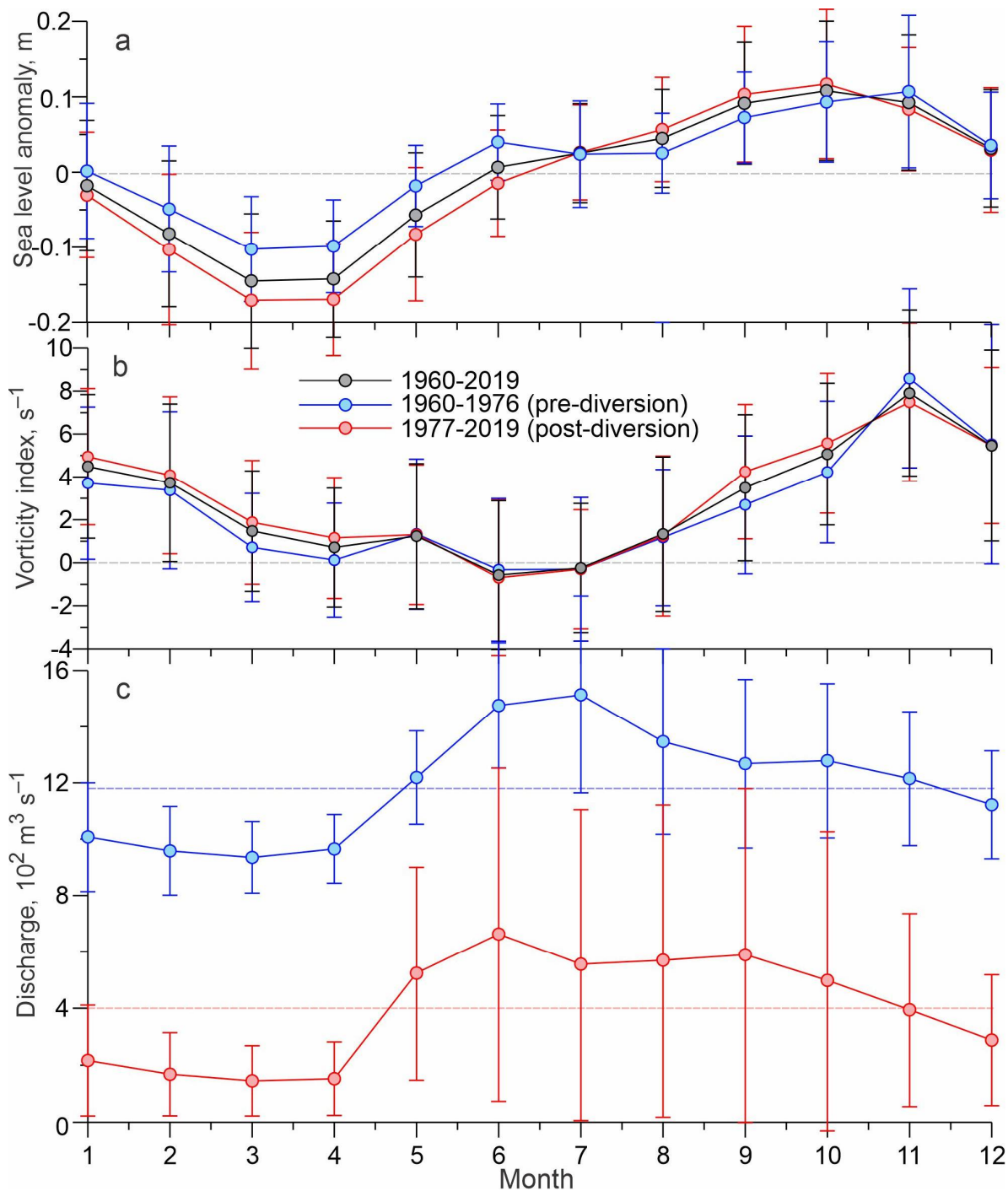


960

961

962 **Figure 4:** (a) 30-day running mean of the Churchill River discharge (black; $10^2 \text{ m}^3 \text{ s}^{-1}$) and
 963 detrended SLA at Churchill (blue; m). Gray circles show mean discharge pre- and post-diversion
 964 with standard deviations depicted with red error bars. (b) Correlation R between daily Churchill
 965 River discharge and SLA computed for the 365-day moving window (black) with their 365-day
 966 running mean (red). Pink shading highlights statistically insignificant correlations at the 99%
 967 confidence level. Numbers at the top show correlation between daily Churchill River discharge
 968 and SLA computed for 1950-1976 and 1977-2018 pre- and post-diversion, respectively. (a, b)
 969 Yellow shading highlights August-May 1969-70 and 2003-04. Black arrow indicates onset of the
 970 Churchill River diversion. Gray shading highlights periods when the sea level seasonal cycle was
 971 partially disrupted (1981-82 and 1987-88), or significantly diminished (1962-63 and 2016-2017).

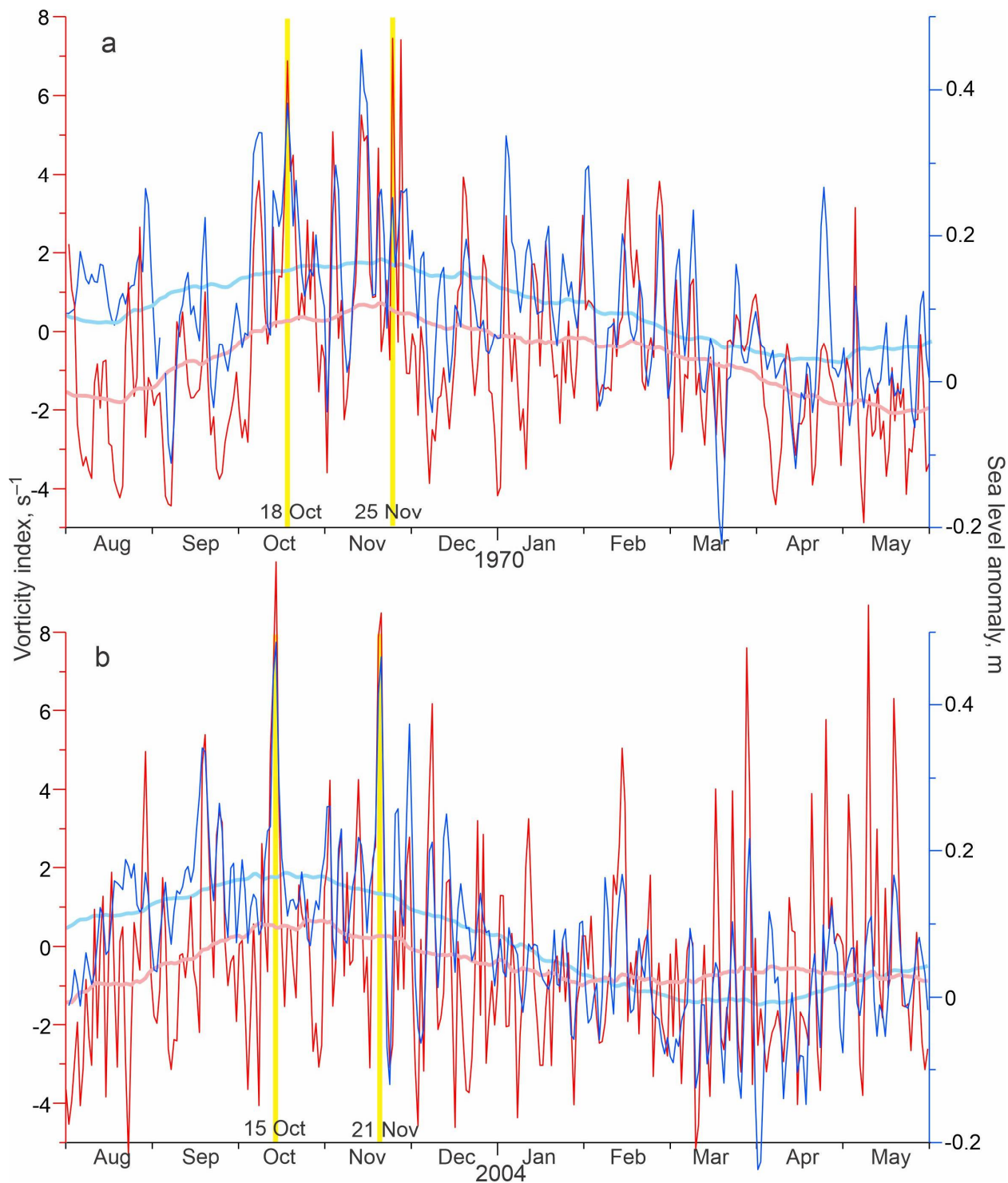
972



973

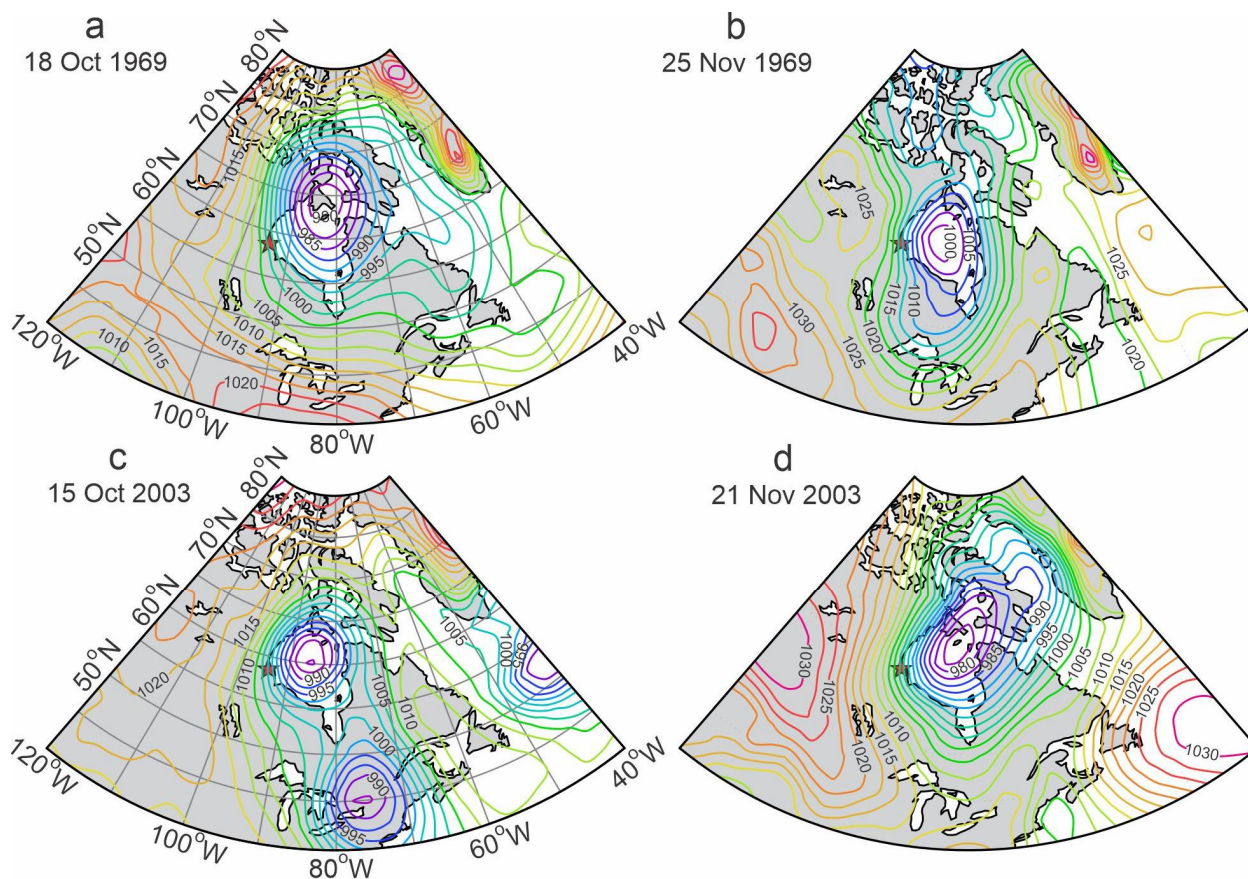
974 **Figure 5:** Seasonal cycle of (a) SLA at Churchill (m), (b) atmospheric vorticity over Hudson
 975 Bay (s^{-1}), and (c) Churchill River discharge ($10^2 m^3 s^{-1}$). Seasonal cycle derived using monthly-
 976 mean data for (a, b) 1950-2019 (black), (a, b) 1950-76 (blue) and (c) 1960-76 (blue) before the
 977 Churchill River diversion, and (a, b, c) 1977-2018 (red) after the Churchill River diversion. Error
 978 bars show \pm one standard deviation of the mean. (c) Blue and pink dashed lines show the long-
 979 term mean discharge before and after diversion, respectively.

980



981
 982 **Figure 6:** Time series of the daily mean vorticity index (red; s⁻¹) and SLA at Churchill (blue; m)
 983 with their 91-day running mean in pink and light blue, respectively, for August/May (a)
 984 1969/1970 and (b) 2003/2004. (a, b) Vertical yellow lines highlight coherent peaks in vorticity
 985 and sea level in October and November.

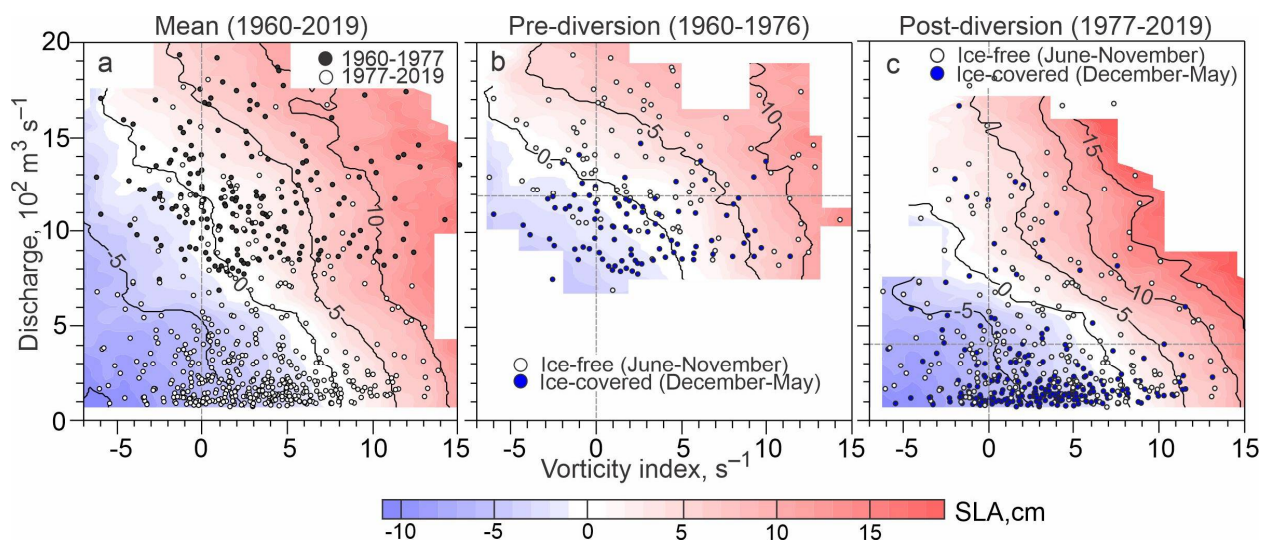
986
987
988
989
990



991
992
993
994
995

Figure 7: Sea level atmospheric pressure (hPa) for coherent peaks in atmospheric vorticity and sea level at Churchill, highlighted in Figure 6 with yellow lines: (a) 18 October 1969, (b) 25 November 1969, (c) 15 October 2003, and (d) 21 November 2003.

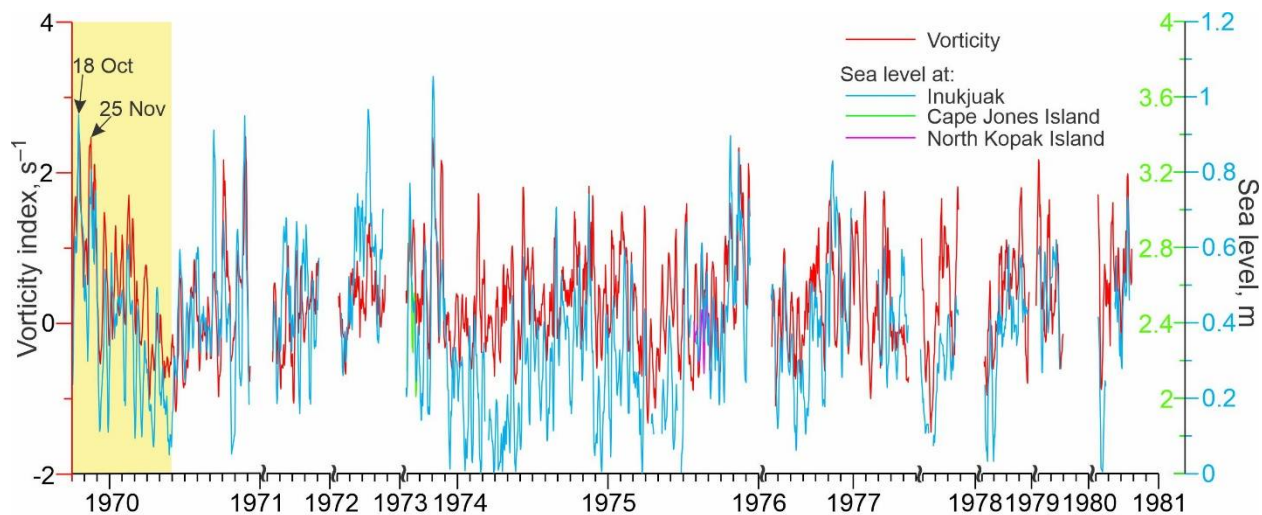
996
997
998
999
1000
1001
1002



1003
1004
1005
1006
1007
1008
1009
1010
1011
1012
1013

Figure 8: Color shading shows monthly mean sea level anomalies (cm) from tidal gauge at Churchill versus atmospheric vorticity (s^{-1} ; horizontal axis) and Churchill River discharge ($10^2 m^3 s^{-1}$; vertical axis) for (a) entire period of river discharge observations (1960 – 2019), and (b) before and (c) after the Churchill River diversion in 1977. Scatter plots show monthly mean vorticity and river discharge for (a) 1960-1976 (black circles) and 1977-2019 (white circles), and (b, c) ice-free season (June-November; white circles) and ice-covered season (December-May; blue circles). Horizontal gray dashed line shows mean river discharge (c) before and (d) after diversion.

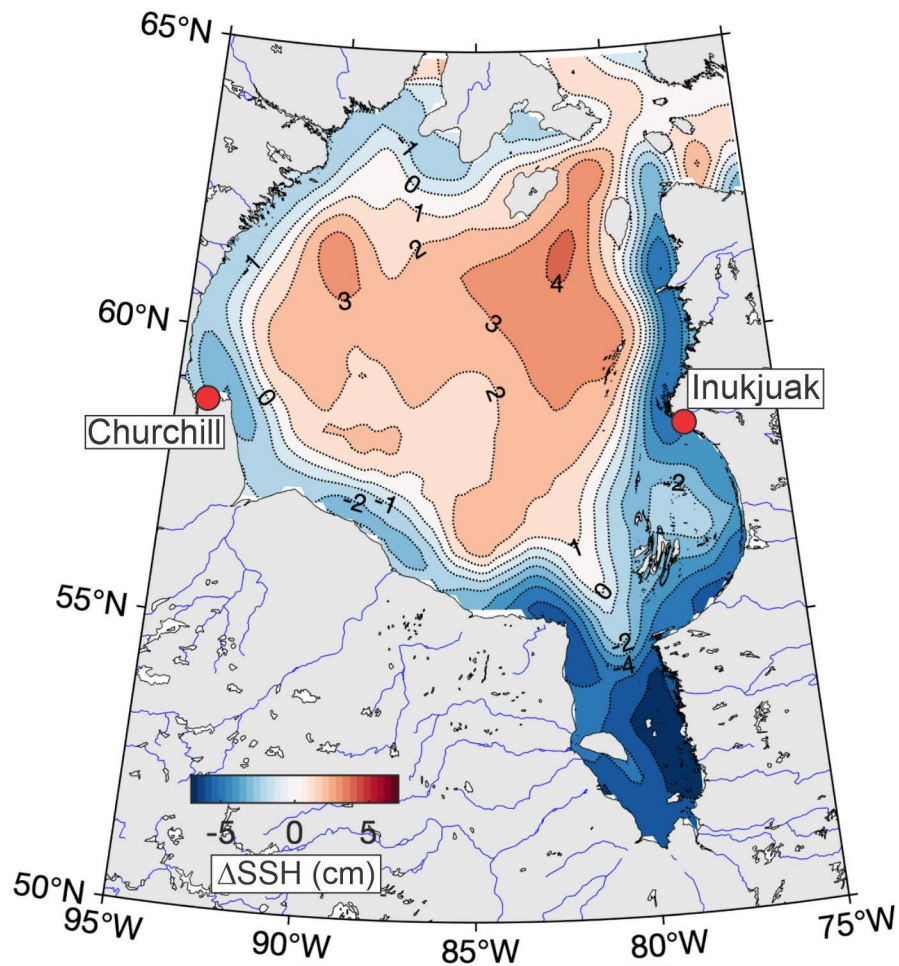
1014
1015
1016
1017
1018
1019



1020
1021
1022
1023
1024
1025
1026
1027

Figure 9: Time series of 7-day running mean for daily atmospheric vorticity index (red, s^{-1}) over Hudson Bay and daily mean sea level (m) measured at the tide gauge in Inukjuak (blue), Cape Jones Island (green) and North Kopak Island (purple). Yellow shading highlights October/May 1969/70. Black arrows indicate two cyclonic storms in 18 October and 25 November 1969 with atmospheric forcing shown in Figures 7a and 7b, respectively. Right vertical axis shows sea-level scale for Inukjuak (blue), and Cape Jones Island and North Kopak Island (green).

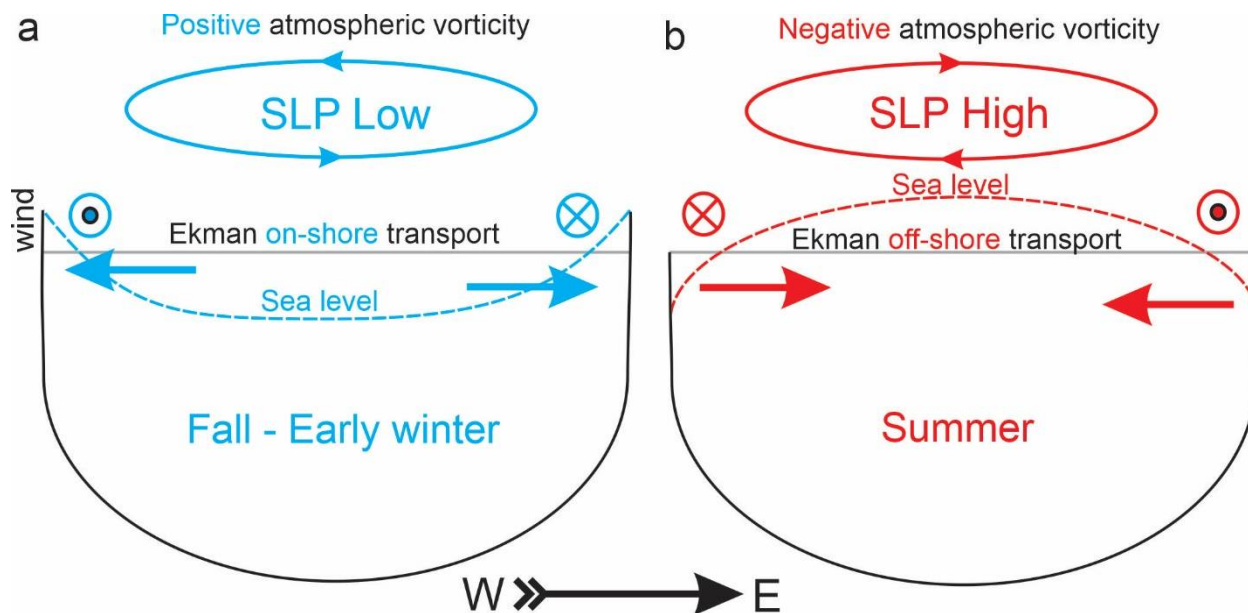
1028
1029
1030
1031



1032
1033
1034
1035
1036

Figure 10: The long-term mean (1993-2020) difference between sea surface height (SSH; cm) in summer (June-August) and fall (September-November) derived from the satellite altimetry. Red dots depict the tide gauge in Churchill and Innukjuak.

1037
1038
1039
1040
1041
1042



1043
1044
1045
1046
1047
1048
1049
1050
1051

Figure 11: Diagram of the proposed impact of the seasonal changes in atmospheric vorticity on the sea level seasonal variability in Hudson Bay. (a) Positive (cyclonic) vorticity during October-December causes onshore Ekman transport and storm surges over the coast. (b) Negative (anticyclonic) vorticity during June-July forces offshore Ekman transport. During winter, a complete sea-ice cover reduces momentum transfer from wind stress to the water column diminishing impact of atmospheric forcing on sea level variability. Dotted and crossed circles depict southerly and northerly along-shore surface winds, respectively.